THESIS FOR THE DEGREE OF DOCTOR OF PHILOSOPHY

Mixing of Large Solids in Fluidized Beds

Semiempirical Modeling and Experiments with Application to Fuel Mixing

ANNA KÖHLER

Department of Space, Earth and Environment
CHALMERS UNIVERSITY OF TECHNOLOGY

Gothenburg, Sweden 2021

Mixing of Large Solids in Fluidized Beds
Semiempirical Modeling and Experiments with Application to Fuel Mixing
ANNA KÖHLER
ISBN 978-91-7905-509-7

Doktorsavhandlingar vid Chalmers tekniska högskola
Ny serie nr 4976
ISSN 0346-718X

Department of Space, Earth and Environment
Division of Energy Technology
Chalmers University of Technology
SE-412 96 Gothenburg
Sweden
Telephone +46 (0)31-772 1000

Title page: Schematic of the model for the motion of a large particle in the three different zones identified in a fluidized bed: (1) the gas-solids emulsion with sinking bulk solids; (2) the bubble wake zone with rising bulk solids; and (3) the splash zone. In the lateral direction, the bed is divided into recirculation cells. A large particle in the emulsion may join a bubble wake. Bubble eruption at the bed surface leads to ejection of the particle, which lands back on the bed surface.

Printed by Chalmers Reproservice
Chalmers University of Technology
Gothenburg, Sweden 2021

Above all, don't fear difficult moments.
The best comes from them.
Rita Levi Montalcini

Vet du, jag är inte rädd.
Jag är bara inte riktigt van.
Gustav, 6 år.

Mixing of Large Solids in Fluidized Beds

Semiempirical Modeling and Experiments with Application to Fuel Mixing

ANNA KÖHLER
Division of Energy Technology
Department of Space, Earth and Environment
Chalmers University of Technology

Abstract

Fluidization is a technology that is widely used in systems in which particulate solids are to be transported, mixed, and/or reacted with gases. In fluidized bed applications, the lateral mixing rate of the solids and the heat and mass transfer with their surroundings play important roles in process performance. These transport mechanisms are affected by the solids axial mixing, as particles immersed in the dense bed will experience higher levels of heat transfer, lower mass transfer, and lower rates of lateral mixing than they would if floating on the bed surface. However, there is a lack of knowledge regarding the effects of the solids properties and operating conditions on the solids mixing. As a consequence, there is a lack of predictive tools that can be used for optimizing the design and operation of fluidized beds.

This work focuses on advancing the current understanding of the mixing of large solids (typically fuels) in fluidized beds, with the aims of promoting the design of new applications and improving the scale-up and operation of commercial units. While a generic approach is adopted in terms of considering a wide range of solid particle properties (size and density), the focus is on biomass particles, for which thermochemical conversion fluidized beds are especially suited, due to their: high-level fuel flexibility (being able to convert efficiently low-grade fuels); ability to control emissions with in-bed methods; and inherent capability to capture CO_2 with looping dual fluidized bed systems.

This work combines semiempirical modeling with experiments that apply magnetic particle tracking in a fluid-dynamically downscaled bed, enabling the closure as well as the validation of the model. By deriving a mechanistic description of the motion of a spherical object, the model identifies key parameters that are crucial for describing the mixing. Among these, the effective drag of the bed emulsion acting on the fuel particle is further studied in dedicated experiments with falling and rising tracers in various types of beds at minimum fluidization. The stress patterns observed in these rheological experiments reveal a non-Newtonian behavior of the drag between the bed emulsion and immersed larger objects. This is then implemented in the model for further upgrading of the mechanistic description. The model is shown to describe ably both axial mixing and the lateral mixing of different fuel types under conditions applicable to industrial-scale hot units.

The combination of modeling and experimental work shows that while axial mixing is fostered by increasing the fluidization velocity, bed height, distributor pressure

drop, or fuel particle density and decreasing the fuel particle size, only a higher fluidization velocity exerts a clear influence on the lateral dispersion. This can be explained in terms of the influence of the fluidization velocity on the width of recirculation cells, which are found to play a major role in the lateral mixing of fuel particles and warrant further study.

Keywords: fluidized beds, fuel mixing, semiempirical modeling, magnetic particle tracking, fluid-dynamic downscaling, drag

Acknowledgments

Despite spending a decent amount of time in Swedish nature, pursuing a Ph.D. has probably been one of my biggest adventures. This is to the people, who have made the journey not only possible and but also very enjoyable.

Henrik, thank you for enabling this project, your enthusiasm, and ideas that always give my work a wider perspective. Filip, thanks for your great interest in my project. With your vast experience in the field, it is ever-evolving to get your feedback.

David, thank you for your inexhaustible dedication to my development, both as a researcher and as a person. With a compass always pointing to the summit and your subtle intuition for when the weather changes, you have saved this trip numberless times. Thank you for being my mentor and inspiration during all these years.

Carolina, although just joined for the last leg of the journey, you have become indispensable to me from day one. Your ability to fix equipment with a flick of the wrist and your Austrian-Colombian army knife has left me deeply impressed and your ever-good mood has lightened up my Ph.D. life since your arrival.

Anna, my twin from the South, thank you for the joyful discussions about programming and drag formulas, and the introduction to real chocolate spread.

To Antonio and Eduardo from UC3M, thank you for the great collaboration on the modeling paper. It was such a fruitful experience to work with you.

I would like to thank Jessica, Ulf, and Rustan, and our dear colleagues from Acreo, who were involved in the experimental part of my work. Rustan, your structured and creative way of solving technical problems in the lab was worth a mint for me.

To my fellow Ph.D. students and colleagues, how have I missed meeting you all at the division during this last year. Thank you for staying in touch besides these adventurous times. A special thanks to the one and only A-team for all the help I got from you since I started at the division.

With special times come special acquaintances. Thank you to my friends in Tösakull for all the time we spent together during this year. To my friends and family, who shared the thrill with me from Germany and Switzerland, I'm very grateful for your support. To my Swedish family, thank you for making me feel at home in Skortebo, for being that place, where I can just be.

My dear Anders, thank you for always being with me on this journey. On the rocky road of life, I cannot think of something better than feeling my hand in yours while walking side by side with you.

This work has been financed by the Swedish Gasification Centre (SFC) within the framework of the Centre for Indirect Gasification of Biomass (CIGB).

Anna Köhler
Gothenburg, May 2021

Thesis

List of Publications

This thesis comprises an extended summary and the following papers, which are referred to in the text by their Roman numerals:

I. A. Köhler, D. Pallarès and F. Johnsson. Modeling Axial Mixing of Fuel Particles in the Dense Region of a Fluidized Bed. Energy & Fuels, 2020, 34 (3), 3294-3304.

II. A. Köhler, E. Cano Pleite, A. Soria-Verdugo, D. Pallarès and F. Johnsson. Modeling the motion of fuel particles in the bottom region of a gas-fluidized bed. *Submitted for publication. Under review.*

III. A. Köhler, D. Pallarès and F. Johnsson. Magnetic tracking of a fuel particle in a fluid-dynamically down-scaled fluidised bed. Fuel Processing Technology, 2017, 162, 147-156.

IV. A. Köhler, A. Rasch, D. Pallarès and F. Johnsson. Experimental characterization of axial fuel mixing in fluidized beds by magnetic particle tracking. Powder Technology, 2017, Volume 316, 492-499.

V. A. Köhler, D. C. Guío-Pérez, A. Prati, M. Larcher and D. Pallarès. Rheological effects of a gas fluidized bed emulsion on falling and rising spheres. *Submitted for publication. Under review.*

VI. D. C. Guío-Pérez, A. Köhler, A. Prati, D. Pallarès and F. Johnsson. Effective drag on spheres immersed in a fluidized bed at minimum fluidization - influence of bulk solids properties. *To be submitted.*

Contribution report

Anna Köhler is the principal author of **Papers I**–**V**, with responsibility for the planning and formulation of the publications. She was the main person responsible for the formulation of the axial model, the validation of the models, and the data evaluation for **Papers I** and **II**, as well as for the planning and execution of the experimental work and data evaluation of **Paper III**. For **Papers IV** and **V**, she was responsible for the planning of the experiments and the analysis of the data. As second author of **Paper VI**, she supported the preparation and execution of the experiments and contributed to the data analysis and the manuscript with discussions and ideas.

Dr. Eduardo Cano Pleite realized the implementation of the axial model into the lateral model, and contributed with discussions and ideas to **Paper II**. Associate Professor Antonio Soria-Verdugo formulated the original lateral model and contributed with discussions and ideas to **Paper II**. Bachelor degree student Alexander Rasch conducted the experiments described in **Paper IV**. Dr. Diana Carolina Guío-Pérez is the principal author of **Paper VI** and was responsible for the planning of the experiments, data evaluation and formulation of the paper. She supported the preparation and execution of the experiments and contributed with discussions and ideas to **Paper V**. Doctoral student Anna Prati supported the preparation, execution and analysis of the experiments described in **Papers V** and **VI**. Associate Professor Michele Larcher contributed with discussions and revision to **Paper V**. Associate Professor David Pallarès, who is the main supervisor of this work, contributed to the experimental and modeling work with ideas, discussions and guidance, and with the editing and revision of all six publications. Professor Filip Johnsson has contributed with discussions, and guidance, as well as the editing of **Papers I**–**IV** and **Paper VI**.

Publications not included in this work

Additional publications related to the work are listed below but have not been included in the thesis, as they are either outside the scope of this thesis or overlap with the appended articles.

1) E. Sette, A. Köhler, D. Pallarès and F. Johnsson. Modeling Axial 3-dimensional particle tracking in a fluid-dynamically downscaled fluidized bed using magneto resistive sensors. *The 8th International Symposium on Coal Combustion, Beijing, China, 2015.*
2) A. Köhler, D. Pallarès and F. Johnsson. Modelling Axial Mixing of Char – Application to the Dense Bottom Bed in CFB Boilers. *12th International Conference on Fluidized Bed Technology, Krakow, Poland, 2017.*
3) A. Köhler, D. Pallarès and F. Johnsson. Determination of the Apparent Viscosity of Dense Gas-Solids Emulsion by Magnetic Particle Tracking. *23rd International Conference on Fluidized Bed Conversion, Seoul, Korea, 2018.*

To my mother.

Contents

Nomenclature

The following list (in alphabetic order) explains the acronyms and abbreviations, as well as Greek and Latin symbols used in the thesis.

Definitions

Bingham plastic	Fluid with a yield stress and constant viscosity
Gulf streaming	Toroidal flow pattern of the bulk solids
Non-viscous fluid	Non-Newtonian fluid
Recirculation cell	Cell of bulk solids flow, formed around bubble path
Rheogram	Diagram of shear stress vs. shear rate
Throughflow	Additional gas flow flowing through bubbles and emulsion
Viscoplastic	Shear-thinning fluid with yield stress
Viscous fluid	Newtonian fluid, fluid with a viscosity
Yield stress	Non-zero shear stress at zero shear rate

Abbreviations and Acronyms

0D	Non-dimensional
1.5D	One-and-a-half-dimensional
1D	One-dimensional
2.5D	Two-and-a-half-dimensional
2D	Two-dimensional
3D	Three-dimensional
BFB	Bubbling fluidized bed
CFB	Circulating fluidized bed
CGP	Composite Gaussian process
CL	Chemical looping
CO_2	Carbon dioxide
DFB	Dual fluidized bed
DNS	Direct numerical simulation
DPM	Discrete phase model
E-E	Eulerian-Eulerian
E-L	Eulerian-Lagrangian
FB	Fluidized bed
G	Giga
GHG	Greenhouse gas
GROT	*Grenar Och Toppar* (branches and tree tops)

MP-PIC	Multiphase particle-in-cell method
MPT	Magnetic particle tracking
PEPT	Positron emission particle tracking
PSD	Particle size distribution
RPT	Radioactive particle tracking
SFC	Swedish Gasification Centre
TFM	Two-fluid model

Latin Symbols

a	Acceleration, m/s^2
A_0	Bubble catchment area, m^2
C_D	Drag coefficient, -
D	Dispersion coefficient, m/s^2
d	Diameter, m
f_2	Empirical expression, -
f_w	Bubble wake fraction, -
g	Gravitational acceleration, m/s^2
H	Fixed bed height, m
L	Length, m
m	Mass of fuel particle, kg
q	Probability to start rising, %
Re	Reynolds number, -
t	Time, s
u	Velocity, m/s
x	Length, m
Y	Normalized shear stress, -
z	Axial position, m

Greek Symbols

α	Particle-to-bubble velocity ratio, -
δ	Bubble fraction, -
$\dot{\gamma}$	Shear rate, 1/s
μ	Dynamic viscosity, Pa s
φ	Angle, angular displacement, $^\circ$
ϕ	Sphericity, -
ρ	Density, kg/m^3
τ	Shear stress, Pa
θ	Angle, radial displacement, $^\circ$

Indices

0	Initial
b	Bubble
bed	Bed
br	Single bubble
eff	Effective
em	Emulsion
f	Fluid
lat	Lateral
mf	Minimum fluidization
p	Large particle
s	Bulk solids
tf	Throughflow
vis	Visible

Part A

Extended Summary

1 Introduction

In light of the current climate emergency, with human activities causing the depletion of resources, accumulation of waste, and global temperature increase, the need for drastic reductions of anthropogenic CO_2 emissions through transitioning energy and land use to greater sustainability is unavoidable if we want to stay within the 1.5°C limit for global warming [1]. The heat and power and the industry sectors account for 65% of the global greenhouse gas (GHG) emissions (22 $GtCO_2$), with the vast majority originating from thermal conversion of solid fuels, such as coal [2], which are traditionally used due to their stable and reliable conversion processes, abundance, and relatively low extraction and transport costs.

Among the conventional technologies used for the commercial conversion of solid fuels, such as simpler grate firing, pulverized coal-fired burners and fluidized beds (FBs), the latter stand out as conferring a number of important advantages for the transition to more sustainable energy systems, not least when considering the reduction of GHG emissions, as described in the next section.

1.1 Fluidized bed applications for solid fuel conversion

Fluidization is the dynamic fluid-like state that develops as a gas (or liquid) passes through a bed of particulate solids. Originally patented in the 1920s as the Winkler process for the gasification of coal [3], fluidization is today a widely used technology. FB units can be found in all kinds of applications, ranging from physical operations, such as the feeding, filtering, drying and coating of particles, to different solid-catalyzed processes, such as cracking and reforming, to gas-solid reactions, such as those involving the conversion of solid fuels in combustion and gasification processes [4]. All of these processes require the transportation and/or frequent mixing of the particulate solids, with special emphasis on the transfer of heat and mass with the fluidizing medium. This, together with a high level of versatility, makes fluidization a suitable basis for a number of applications, which are developed to address some of today's most pressing issues in terms of energy sustainability.

Regarding FB processes that contribute to the transition of the energy system towards sustainability, a relatively new process involves the coating of carbon nanotubes in atomic layer deposition reactors [5], which are used in numerous applications coupled to renewable energy systems, such as batteries, solar cells, hydrogen storage and fuel cells [6]. Furthermore, FBs are envisioned to play key roles in large-scale solutions for thermal and thermochemical energy storage systems [7,8]. Regarding the thermo-

chemical conversion of fuels, FB combustion was adopted widely during the 1970s and 1980s [9], thanks to the possibility to enable in-bed reductions of polluting emissions, such as sulfur oxides, through the use of solids sorbents and the low levels of nitrogen oxides linked to the even and low combustion temperatures [10, 11]. Over the last few decades, other advantages of the technology – its fuel flexibility and especially its ability to handle low-grade fuels – have enabled a promising shift away from fossil fuels towards more sustainable fuels [12]. FB conversion processes, e.g., combustion and gasification, can be efficiently run with carbon-neutral fuels such as biomass, as well as with renewable fractions of municipal and industrial wastes [9,13–15], without the need for extensive fuel preparation. An overview of the most common renewable fuels that are amenable to conversion in FB reactors, together with the associated challenges, is given in 1.1.

There are two main types of FB reactors for the conversion of solid fuels: bubbling fluidized beds (BFBs), and circulating fluidized beds (CFBs). The simpler BFBs (typically yielding a specific capacity of around 1 MW/m^2) are preferentially used in plants that have lower thermal capacities, i.e., typically fed with local fuels that have a low energy density so as to avoid costly transportation. In Sweden, BFBs are the predominant boiler type used for district heating, as well as in the pulp and paper industry, with about 3800 MW_{th} capacity installed [16]. CFBs yield higher levels of specific fuel conversion for a given cross-sectional area of the reactor with an output up to 4–5 MW/m^2, representing approximately 2600 MW of installed capacity in Sweden [16]. Since CFBs are associated with higher installation and operational costs, they are traditionally used for large-scale applications, such as coal combustion, with outputs in the range of several hundreds of megawatts [17]. Still, biomass is a commonly used fuel in CFB combustors and gasifiers, both as the sole fuel and for co-firing with coal [16, 18, 19].

With the goal to abate CO_2 emissions, interest in dual fluidized bed (DFB) systems, which allow the solids looping between two FB reactors, has increased, sparking new more-sustainable applications. DFB processes have the major advantage that even though the bed material is circulated between the two reactors, thereby transporting mass and heat, the gas streams in each of the reactors remain separated. An example of this is the chemical looping (CL) process, in which an oxygen carrier is looped to enable inherent capture of CO_2 without a major energy penalty in any of its different variants (combustion, gasification, and reforming [20, 21]). In a similar manner, calcium looping applies a calcium oxide as the oxygen carrier in two CFBs [22], so as to capture CO_2 in, for example, the calcination step of the cement production, which accounts for about 60% of the total emissions of this carbon-intense process [23]. Regarding the application of DFBs using inactive bed materials, indirect gasification of biomass [16] is used for the generation of a raw biogas with high heating value by combining a gasifier with a CFB combustor, which serves as a heat source for the endothermic reactions in the gasifier.

Table 1.1: Carbon-neutral solid fuels derived from biomass and waste [24].

Product		Definition	Examples (Possible challenges)
Biomass	Woody biomass	Biomass originating from trees.	Firewood, pellets, wood chips (High moisture and volatiles content)
	Wood waste	Waste from wood processing industry (pulp and paper, saw mills).	Black liquor (liquid, smelt formation), sawdust (fine powder), bark & GROT (irregular shapes, high moisture content)
	Agricultural residues	Residuals from maintenance, cropping and processing of plants.	Straw, vegetable husks, nut shells (Low ash melting point, N/S/Cl contents)
	Municipal waste (biogenic)	Biogenic part of waste from households and industries, collected by local authorities.	Paper, cotton, food waste (irregular size, high moisture content)
	Animal waste	Excreted materials from live stock (animals and humans).	Animal manure, human sewage
	Charcoal	Solid residue from pyrolysis of biomass. As a secondary product charcoal is often treated differently.	Charcoal, briquettes
Industrial waste		Residues of non-renewable from industrial processes (chemical processes, manufacturing).	Plastics, tyres, ASR
Municipal waste		Non-biogenic part of waste produced by households and industries, collected by local authorities.	Burnable household waste, packaging (irregular size, high moisture content)

Firewood is mainly fired in small scale heating boilers.
GROT: GRenar Och Toppar, Swedish for "branches and (tree) tops". ASR: Automotive Shredder Residues

With the diverse applications of FBs for the thermochemical conversion of solid fuels, and the increased interest in alternative fuels and in the reduction of CO_2 emissions, new challenges related to the design of FBs have emerged.

1.2 Fuel mixing in fluidized bed reactors

Figure 1.1 exemplifies the different processes in the bottom region of a FB reactor used for solid fuel conversion, and illustrates how fuel mixing relates to the different mechanisms. As gas is fed over the whole cross-section of the bed through a bottom distributor, the bulk solids are fluidized, and bubbles are formed. These bubbles grow as they ascend through the bed, inducing mixing of the bed solids, and eventually ejecting solids into the freeboard as they erupt on the bed surface. Solid fuels (consisting of moisture, volatiles, char, and ash) are fed through ports located on the sidewalls of the reactor. As they are being converted, fuel particles spread over the cross-section of the reactor (lateral mixing) and over the height of the bed (axial mixing), with increasing gas flows fostering more vigorous mixing of the solids [25]. Axial and lateral mixing are key processes for the successful design and operation of FBs, as discussed in more detail below.

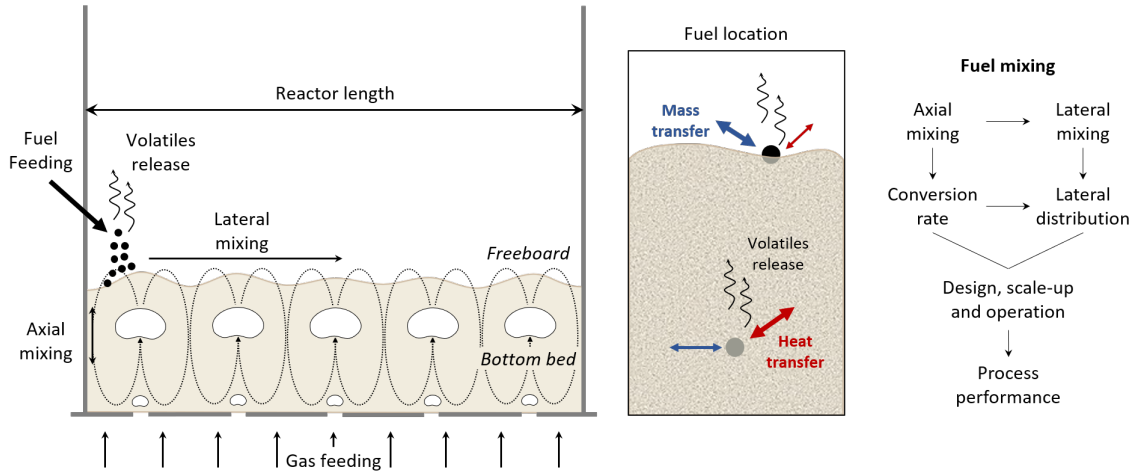

Figure 1.1: Solid fuel mixing and conversion processes in the bottom region of a FB reactor.

BFB reactors are typically operated in the bubbling fluidization regime, i.e., as the gas velocities are low, the bulk solids fall back onto the bed surface and no significant amounts of solids are entrained into the transport zone of the reactor. In CFBs, fluidization velocities are high, typically exceeding the terminal velocity of the bulk solids, such that the solids are entrained into the upper freeboard, with some of them eventually leaving the riser and having to be circulated back through return systems (consisting mainly of cyclones and loop seals). Despite their differences in design and operational conditions, the bottom regions of BFBs and CFBs yield similar

behaviors in terms of fluid dynamics, with bubbles rising through the bed causing vigorous mixing of the solids (including the fuel particles) [26].

Regarding lateral mixing of the fuel, commercial-scale FB units for solid fuel conversion have cross-sections that span tens of square meters, over which the fuel particles should be distributed evenly to enable efficient conversion. However, with drying and devolatilization times being short (a few tens of a second for typical FB fuels and conditions [27]), the accumulation of high concentrations of volatile matter close to the fuel feeding ports is a common problem in that it divides the reactor into oxygen-poor and oxygen-rich areas, especially when converting fuels that have a high content of volatiles, such as woody biomass [28, 29].

In combustors, this maldistribution of gas species can result in temperature and emission peaks [10, 30], and carries a risk of volatiles burn-out outside the riser. As for gasification, large amounts of rapidly released volatiles have been linked to high yields of unwanted tars in the product gases [29], with the extent of mixing of the volatiles, likewise, being the limiting factor for fuel conversion. As biomass stores up to 68% of its carbon content and 80% of its heating value in the volatile matter, operational strategies to enhance lateral fuel mixing are usually planned for both combustors and gasifiers [31, 32].

Moreover, in DFB systems, the circulation of solids between the reactors creates a macroscopic convective flow of bed material, which is superimposed onto the dispersive lateral mixing of the bed material and fuel particles [33]. In DFBs, excessive rates of lateral mixing can lead to residence times of the fuel (and most critically, of the char) that are insufficient for their full conversion within the reactor. In turn, lateral mixing is influenced by the axial location of the fuel particles, i.e., fuel particles that are floating on the bed surface will spread faster in the lateral directions than fuel particles immersed in the bed [34].

This is critical for the design of FB units, as for instance when determining the optimal number and location of fuel feeding ports [35,36], so as to minimize the issues mentioned above.

Axial mixing not only affects the residence time of the fuel particles in the reactor, but it has also a strong impact on the rates of fuel conversion (Figure 1.1). Fuel particles that are immersed in the dense bed will experience a higher heat transfer rate than those floating on the bed surface [37], entailing shorter drying and devolatilization times, which have been shown to yield a more-reactive char [38]. In contrast, mass transfer between the reactive gas species and immersed fuel particles will be hindered by the bulk solids, yielding lower rates for mass-transfer-driven processes, e.g., the combustion of large char particles. In the case of catalytic bed materials being used, the benefits of operational strategies to keep the fuel immersed in the dense bed have been reported [32]: devolatilization of immersed biomass increases contacts between the volatile gases and solids, significantly reducing the tar yield in the product gas.

Fuel mixing in FBs is influenced by several factors, such as the properties of the bed material and the fuel particles, the operating conditions, and the properties of the fuel (for a summary of these factors, see Figure 1.3). This is because fuel mixing results from a combination of underlying mechanisms (as illustrated in Figure 1.2), starting with the mixing of the bulk solids in the dense bed, which drift along the surface of the ascending bubbles and are pulled upwards in the bubble wakes [39–42]. Eventually, the rising bubbles erupt at the bed surface, ejecting bed material into the freeboard, where it is scattered in the lateral direction [43].

In shallow and wide beds, as are typical for BFBs and CFBs, the bubbles form bubble paths [44, 45] – a stream of rising bubbles trailing along roughly the same path – around which the motion of the bed material forms a toroidal pattern, known as *gulf streaming* [46]. Bed material flows upwards in the (bubble-rich) inner region of the toroid, and flows downwards in the (bubble-poor) outer region of the toroid, to fulfil the mass balance. Fuel particles are, in their turn, dragged by this solids flow. As indicated in Figure 1.2, axial motion of the fuel is characterized by the drag exerted on the fuel particles by sinking solids (a) and rising-wake solids (c) [39,40,44]. The lateral motion of the fuel in the dense bed is induced by the drag into a bubble path (b) or the release from the latter (d), while lateral mixing on the bed surface is caused by the scattering of bubble eruptions (e) [43].

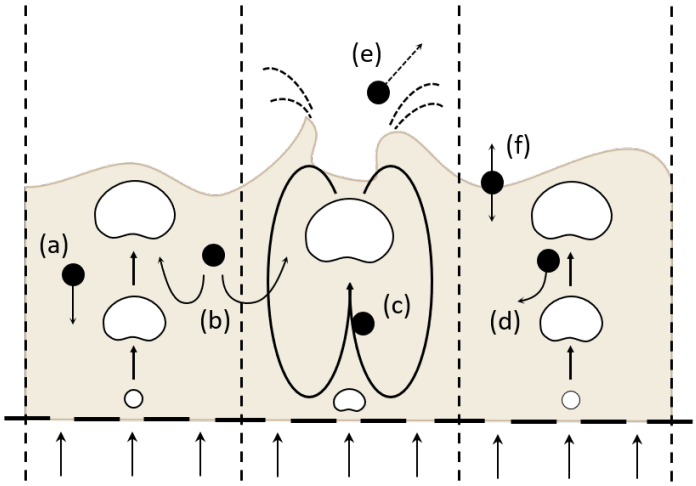

Figure 1.2: Schematic of fuel mixing in the dense bed of a FB with brown fluidized bed solids (emulsion), white rising gas voids (bubbles), and black circulating objects (fuel particles). (a) Sinking fuel particle in the emulsion phase. (b) A sinking particle gets dragged into a bubble path. (c) Fuel particle rising with the wake solids of the bubble path. (d) Particle released from the bubble wake. (e) Fuel particle scattered in the freeboard by bubble eruption. (f) Buoyant fuel particle floating on the bed surface.

The various factors that affect fuel mixing in FBs are summarized in Figure 1.3. As previous studies have primarily focused on processes that use conventional fuels, such as coal and lignite, which have low moisture and volatile contents, high densities, and usually rounder shapes and smaller sizes, there is a general lack of understanding of

the mixing of fuels derived from biomass and waste. Besides the contributions of their larger sizes and lower densities to the typical flotsam behaviors of these low-grade fuels (*cf.* Figure 1.2(f)) [47, 48], their high moisture and volatile contents result in a more-intensive release of gases, which adds buoyancy [28, 49, 50].

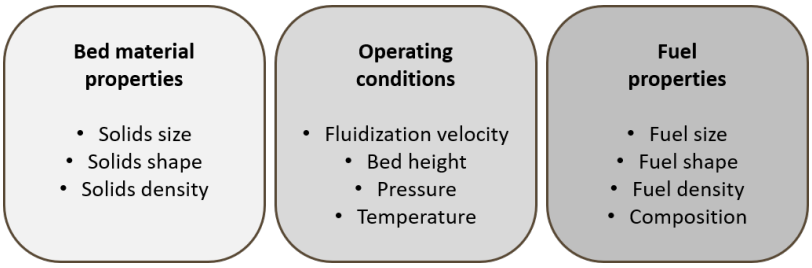

Figure 1.3: Factors influencing fuel mixing in fluidized beds: bed material properties, operating conditions, and fuel properties.

These different fuel properties become important aspects to consider during the design, scale-up, and operation of FB units for solid fuel conversion, which despite their widespread deployment and successful applications, remain mostly as processes with empirical-based development. With the understanding of fuel mixing and its determinant factors being crucial for fuel conversion applications, experiments and models can be useful tools for improving the design, scale-up and operation of FB units.

1.3 Modeling of fluidized beds

Fluidized beds are complex multiphase flow systems that involve momentum, heat and mass being transported within and between different phases over a wide range of lengths and time-scales, which means that measurements and modeling are challenging tasks [51]. In the early period of their development, scarce knowledge and limited computational capacity [52] meant that experimental correlations were the only useful tools for optimizing the design and operation of FBs. As knowledge of this field has expanded and computational power has increased, tools for the predictive design and operation and the modeling of detailed gas-solids fluid dynamics have been developed and refined.

Although not fully established and with variably designated boundaries, the terms micro-, meso- and macro-scale are used in the literature to describe phenomena that range from the particle level (micro), to particle clusters and small flow structures (meso), to large flow structures and phenomena (macro) [31, 53, 54]. Figure 1.4 gives an overview of the different models used for the diverse scales present in an FB, which can be divided into three main types: computational fluid dynamics (CFD); semiempirical models; and empirical correlations [55, 56].

CFD models, which are derived from first principles, provide solutions to generic, governing transport equations (momentum, heat and mass balances) and can be categorized according to their descriptions of the bulk solids. While Eulerian-Lagrangian (E-L) models regard the solids as discrete elements (particle clusters in the case of CGP and MP-PIC) and solve their trajectories, Eulerian-Eulerian (E-E) models treat the solids phase and the gas phase as interpenetrating continua.

Major challenges associated with E-L models relate to their high computational cost. Despite their limitation to spherical particles, they are not applicable for commercial-scale units given the large numbers of bulk solids in these beds and the time-steps required to resolve all particle-particle collisions.

E-E models, in similarity to the two-fluid model (TFM), are based on the kinetic theory of granular flow, which was originally developed to describe the flow of frictionless particles. Therefore, it relies on proper extensions to account for friction and non-binary collisions, as well as the interaction with the gas phase. This is achieved by applying theoretically derived expressions for the solids stress tensor, yielding rather complex models with limited validity. With sufficient computational power being available, CFD TFM models can be useful for investigating phenomena in the meso-scale and macro-scale. However, they are limited to 2D beds and smaller units (10^{-1} m) [57–60].

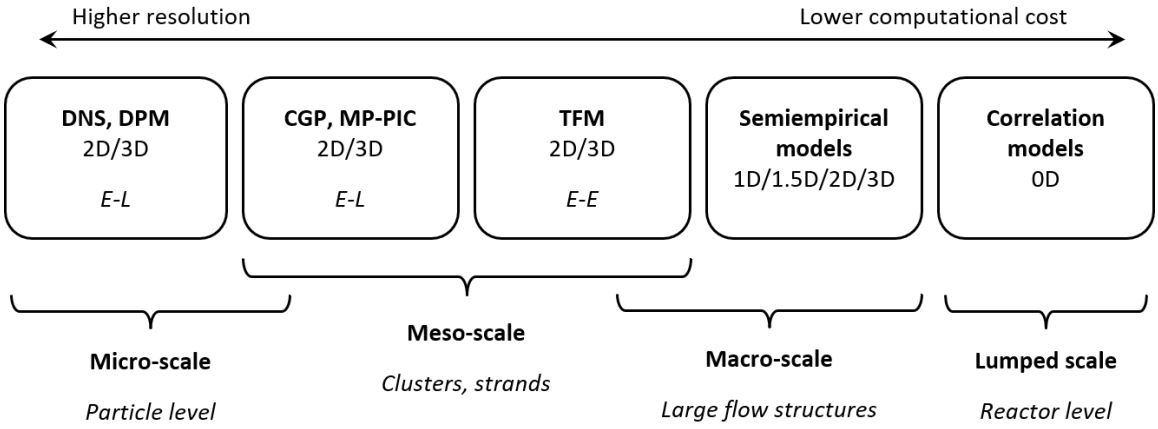

Figure 1.4: Different models for gas-solids flow used to model the diverse phenomena in FBs. The models can be divided into three types: CFD models (E-L/E-E); semiempirical models; and correlation models.

Empirical correlations have a long history of use in fluidization studies, and have been the major modeling type for the scaling-up of FB units [55]. They are typically steady-state 0D models that can provide useful estimations of global variables, such as the heat transfer of the furnace, the flue gas composition, the solids concentration in the boiler, and the outlet temperature.

These correlations are fitted to experimental data. Thus, their validity is typically limited to the operational and geometrical ranges in which the measurements were

made. As the data in the literature originate mainly from experiments performed in small laboratory-scale reactors and data from measurements carried out in hot industrial-scale environments are scarce [31], the transferability of empirical correlations to large units and another operational ranges relies on a strong extrapolation, and is not generally valid. In particular for the design of new applications, the usage of previously developed empirical correlations can be difficult and instead, new experimental data are needed to cover the wider parameter ranges, e.g., the mixing of new fuel types.

Semiempirical (also called *macroscopic*) models usually do not solve the velocity fields of the gas and bulk solids through momentum balances. Instead, they apply simpler sub-models, assumptions or data derived from experiments. These models lack the level of detail of CFD modeling and are somewhat restricted to the range of experimental conditions under which the empirical parameters used were derived. Still, they represent a significant step towards a mechanistic description of FB processes and are being successfully applied in the comprehensive modeling of industrial-scale FBs [54, 61, 62].

Given its affordable computational cost (in the order of hours), semiempirical modeling represents a powerful framework to improve processes of design and scale-up of commercial-scale FB units for the thermochemical conversion of solid fuels. However, literature does not provide validated descriptions for the mixing of fuel particles that could be implemented and exploited in such a modeling framework.

1.4 Thesis overview

1.4.1 Aim and objectives

In summary of the previous sections, with a shift to more sustainable energy processes, the interest in new FB applications and the exchange of fossil fuels with bio-based fuels in existing FB processes is increasing. By affecting major variables (conversion, lateral distribution, residence time) in the bed, the mixing of the fuel is an important parameter during the design process of new units and the scale-up of established reactor designs. Despite its critical importance, there is a lack of reliable descriptions for the fuel mixing in industrial-scale units and knowledge of this topic comes mainly from the limited amount of experimental data and correlations specific to each fuel, unit, and operational condition. There have been attempts to describe fuel mixing through CFD modeling, although the methods are still under development and are not yet computationally affordable for large-scale units.

As a consequence, there is a need for answering the research question of by which factors the mixing of large particles in FBs is influenced and, more importantly, through which mechanisms this influence is governed.

The overarching aim of this thesis is to advance understanding of the mixing of larger solids (typically, fuel particles) in the bottom region (the dense bed and splash

zone) of FB units. With the ambition to promote the design of new FB applications, as well as the up-scaling and optimization of commercial units, the thesis exploits semiempirical modeling combined with experimental methods with relevance for industrial-scale units.

The specific objectives of this thesis are:

1. To establish a validated mechanistic description of the mixing of large particles (with focus on properties representative of fuel) in the bottom region of FBs.

2. To characterize the dependencies of fuel mixing on fuel properties, bed properties and operational conditions, thereby identifying the key parameters and governing mechanisms.

3. To evaluate and improve experimental methods for the validation of models of the fuel mixing with relevance for industrial-scale FBs.

1.4.2 Outline and structure

Figure 1.5 gives an overview over the structure of this thesis with the three main parts being: the semiempirical model (middle column), the dedicated experiments (left-hand column), and the validation experiments (right-hand column).

The semiempirical model is based on a bubble flow description with established correlations from literature, on which a formulation of the particle motion is implemented. Chapter 2 gives the theoretical background on particle mixing in FBs used for semiempirical modeling, and describes the implementation of the model (**Papers I** and **II**). From the formulation of the particle motion, important parameters that govern the mixing but are not sufficiently described in literature were identified.

These key parameters were obtained by means of empirical submodels deducted from dedicated experiments. Chapter 3 describes the experimental work of this thesis, in which magnetic particle tracking was the main measurement technique (Section 3.1). The technique was employed in dedicated experiments with a fluid-dynamically downscaled bubbling bed to characterize the mixing parameters (**Papers III** and **IV**, Section 3.2), as well as in dedicated experiments in incipient FBs to study the drag phenomena (**Papers V** and **VI**, Section 3.3).

To validate the model, experiments in the fluid-dynamically downscaled bubbling bed (**Papers III** and **IV**, Section 3.2) and experiments conducted in industrial-scale BFBs described in the literature were used. After validation, as presented in Chapter 4, the model is used to investigate the different factors that impact mixing, as presented in Figure 1.3. Chapter 5 shows a selection of the results that are contributing to advancing our understanding of the mixing of large particles in FBs.

The results are presented by means of the impact, which the most significant factors of those pictured in Figure 1.3 have on the mixing. Chapter 6 summarizes the major conclusions from this work and the suggests future work.

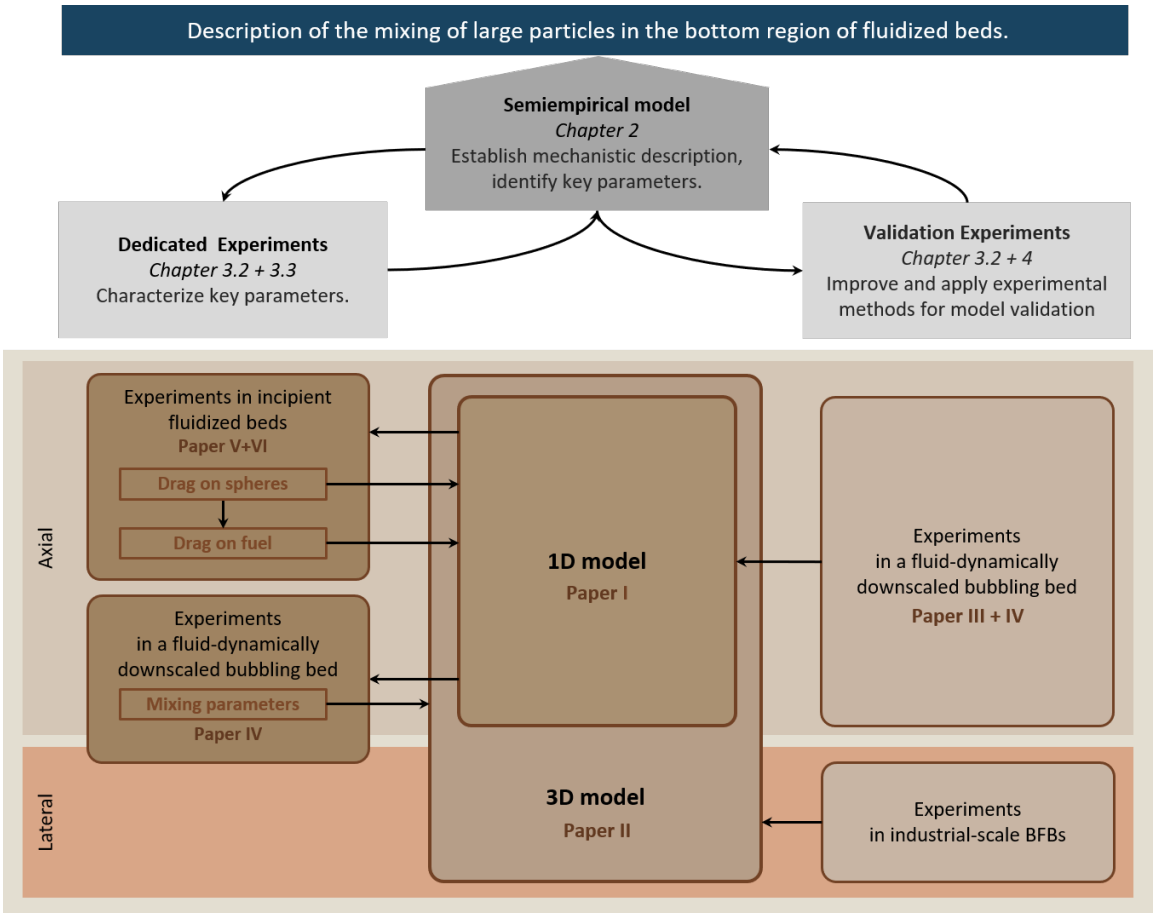

Figure 1.5: Thesis structure. Overview of the research areas, the different methods exploited, and their relationships to the papers included in this thesis.

1.4.3 Context and scope

This work was conducted within the research program of the Swedish Gasification Center (SFC), which aims to develop competence in the field of biomass gasification. It should be noted that this thesis focuses on describing in broad terms the mixing of larger solids in FB units, so that the knowledge attained can also be used for FB applications other than biomass gasification, as long as a non-slugging dense bed is present at the bottom of the reactor and Geldart Group B particles are used as bed material.

The work is fluid dynamical in character, which means that chemical reactions are not considered, although reactions that influence the fluid dynamics are considered indirectly (e.g., the lifting force from the release of moisture and volatiles or the changing densities and sizes of the fuel particles during conversion).

2 Semiempirical model

With the aim to expand the current knowledge of the mixing of large particles in FBs with relevance for industrial scale units, a mechanistic description of the particle mixing is developed using a macroscopic modeling approach (*cf.* middle column in Figure 1.5).

This chapter gives the theoretical background and describes the implementation of the semiempirical model used for simulating the mixing of large particles (typically, fuel particles) in the bottom region of a FB. Descriptions of the model can also be found in **Paper I** (axial mixing model) and **Paper II** (full model for 3D mixing).

2.1 Theory

While gas-solids FBs may be operated under different regimes, this work is concerned with a shallow bed of Geldart Group B solids, which is operated in the bubbling regime (i.e., non-slugging). In this state, the bulk solids, together with the interstitial gas at minimum fluidization, form a solids-gas emulsion, while gas bubbles build up at the bottom of the bed and grow in size as they rise through the bed, inducing a vigorous solids flow around them. This work describes the gas-solids emulsion as a continuum, while the larger particles (whose mixing is studied) are considered discrete elements. The latter are denoted as *large particles* or *fuel particles* when modeled as such, and as *tracer particles* when tracked in experiments.

Figure 2.1 illustrates the motion of an immersed particle through the three different zones (indicated with Arabic numbers), which are the basis of the model. Inside the dense bed there is a bubble-free gas-solids emulsion zone with sinking bulk solids (1), and a bubble wake zone with rising bulk solids in the bubble wakes (2). In both zones, the bulk solids and the gas exert drag on the large particle. In the splash zone above the bed surface (3), the solids ejected by erupting bubbles at the dense bed surface exhibit a ballistic motion, yielding lateral scattering of both the bulk solids and the large particle.

The combination of these three zones establishes a gulf-stream flow pattern, in which the solids flow is repeated in the lateral direction and which consists of the lateral alignment of recirculation cells of length L, each established around a bubble path. The mechanisms for lateral displacement are indicated with Roman numbers in Figure 2.1. Inside the bed, a large particle in the emulsion zone may be caught up in the wake of a passing bubble (I) according to a probability q. This wake can rise in either the same recirculation cell (Ia) or a neighboring cell (Ib), according to

a probability p. Particles that are ejected into the splash zone by bubble eruptions at the dense bed surface (II) end up falling back onto the dense bed within the same recirculation cell (IIa) or a neighboring cell (IIb), depending on the lateral length of their trajectory. Note that while the change of recirculation cells to another one (i.e., b-alternatives of the two general mechanisms) contributes to the effective macroscopic mixing in the lateral direction, circulation within the same cell (i.e., a-alternatives) yields no such phenomenon.

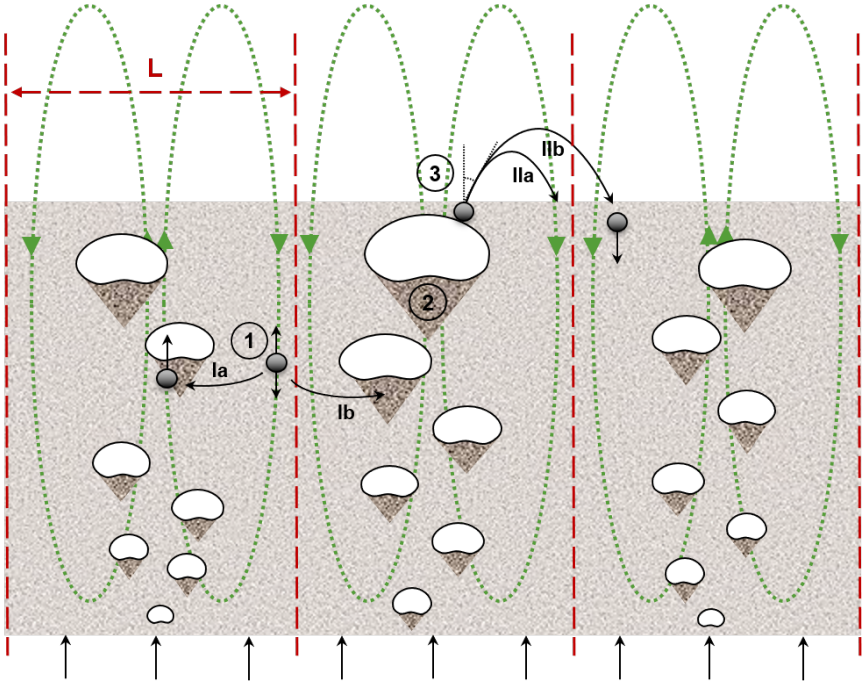

Figure 2.1: Schematic of the model for the motion of a large particle in the three different zones identified in a fluidized bed: (1) the gas-solids emulsion with sinking bulk solids; (2) the bubble wake zone with rising bulk solids; and (3) the splash zone. In the lateral direction, the bed is divided into recirculation cells of length L. A large particle in the emulsion may join a bubble wake, whereby I) the particle starts rising in: a) the same recirculation cell; or b) a neighboring cell. Bubble eruption at the bed surface leads to II) ejection of the particle, which either lands back on the bed surface a) of the same recirculation cell or b) of any other cell.

Gas bubbles are the main driving force for the mixing of bulk solids and fuel particles in FB units. Therefore, the formulation of the model starts with a description of the bubble flow, from which the velocity of the sinking bulk solids and, finally, the motion of the large particles are obtained.

2.1.1 Bubble and bulk solids flows

The initial idea to model the bubble flow in FBs by dividing the gas flow into the bed into two phases (i.e., one bubble phase and one emulsion phase) was presented by Davidson and Harrison [63]. They assumed that one part of the gas flow contributed

to maintaining a minimum fluidization rate in the emulsion phase that contained all the bulk solids, while the remaining gas flow ascended as a solids-free bubble phase [64]. This gas flow model was later extended to include the flow of bulk solids in the bubble wake and cloud [46]. Moreover, under conditions typical for commercial solid fuel conversion units, the two-phase model was found to overestimate the bubble flow, thereby yielding a too-high expansion of the bed, with the result that the presence of a significant gas *throughflow* had to be considered [65–67].

Thus, the total volumetric gas flow into the bed is the sum of the flow at minimum fluidization, the visible bubble flow, and the throughflow. Each of the flows can be expressed per unit area of the bed, treating them in terms of a corresponding gas velocity, with u_0 for the total gas flow, u_{mf} for the flow at minimum fluidization, u_b for the visible bubble flow, and utf for the throughflow. The visible bubble flow can be expressed as the product of the bubble density, δ, and the rise velocity of the bubbles, u_b, such that the gas flow division in the bed expressed as velocities reads as follows:

$$u_0 = u_{mf} + u_{vis} + u_{tf} = u_{mf} + \delta u_b + u_{tf}. \tag{2.1}$$

The bubble rise velocity in beds with multiple bubbles, u_b, is given by superimposing the rise velocity of a single bubble, u_{br}, with the superficial bubble phase velocity [63]:

$$u_b = u_{br} + (u_0 - u_{mf} - u_{tf}). \tag{2.2}$$

Based on an early theoretical derivation of the rising velocity of a single bubble released in a liquid [68], Davidson and Harrison [63] compared different empirical expressions for a single bubble in a large bed at minimum fluidization. From this, they suggested an expression that has subsequently entered common usage:

$$u_{br} = 0.711\sqrt{gd_b} \tag{2.3}$$

where D_b is the equivalent diameter of a sphere with the same volume as the bubble cap. Many different expressions for the bubble diameter are given in the literature [46,47,69,70]. The bubble diameter increases as bubbles rise through the bed, mainly as a result of coalescence with other bubbles. In the present work, the correlation of Darton et al. [69] is used to predict the bubble diameter, which is particularly suitable for freely bubbling beds, considering the growth by coalescence with other bubbles. The correlation reads:

$$d_b = 0.54g^{-0.2}\left(u_0 - u_{mf}\right)^{0.4}\left(z + 4\sqrt{A_0}\right)^{0.8} \tag{2.4}$$

where z is the vertical location of the bubble and A_0 is the bubble catchment area characterized by the spacing between gas-distributing nozzles.

With this the bubble density can be obtained by combining Eqs. 2.1 and 2.2 to give:

$$\delta = \left(1 + \frac{u_{br}}{u_0 - u_{mf} - u_{tf}}\right)^{-1} \tag{2.5}$$

An expression for the throughflow is given in [67], using Eq. 2.5 on the basis of a constant pressure gradient over the bed height, i.e., creating a constant bubble density along the dense bed height:

$$u_{tf} = \left(1 - f_2\left(z + 4\sqrt{A_0}\right)^{0.4}\right)\left(u_0 - u_{mf}\right) \tag{2.6}$$

where f_2 is an empirical expression derived from experiments in a large-scale hot bubbling FB using sand as bed material:

$$f_2 = \left(0.26 + 0.70 \cdot exp\left(-0.0033 d_s\right)\right)\left(0.15 + \left(u_0 - u_{mf}\right)\right)^{-0.33} \tag{2.7}$$

With this, the description of the bubble flow is complete and the velocity of the sinking bulk solids in the emulsion zone can be obtained by fulfilling the continuity of the bulk solids flow over the whole bed. The bulk solids in the bubble wake zone are dragged upwards, inducing a downwards flow of the bulk solids in emulsion zone. Combining the above expressions for the bubble flow (i.e., δ and u_b) with the wake volume fraction of the bubbles, f_w, as given by Kunii and Levenspiel [46], a mass balance over the bed solids in a horizontal bed slice can be formulated. This results in the velocity of the sinking bulk solids in the emulsion zone being expressed as:

$$u_{s\downarrow} = \frac{f_w \delta u_b}{1 - \delta - f_w \delta} \tag{2.8}$$

The values for the wake volume fraction are obtained from cold laboratory-scale experiments using Geldart Group B particles of various sizes and densities [39]. However, as these values seem to be an underestimation of the values seen under conditions representative of hot industrial scale units, this work applies a higher value of 0.63. This was derived by fitting the model to the axial tracer distributions obtained in fluid-dynamically downscaled experiments. This issue is discussed in detail in Section 3.2.

With this, the relevant macroscopic velocities of the bubbles and solids flow can be determined and used to model the motion of a large particle immersed in the bed.

2.1.2 Mixing of large particles

The motion of the large particle is assumed to be governed by the solids flows in the emulsion and bubble wake zones, and the two mechanisms (I and II) indicated

in Figure 2.1. Below, the expressions governing the mixing of a particle in each of the three zones (1: emulsion, 2: bubble wake, 3: splash zone; see Figure 2.1) are presented.

Emulsion zone
The acceleration of the large particle in the emulsion zone is calculated through the equation of motion from the sum of the forces acting on it, with a drag force exerted by the surrounding emulsion bulk solids, which sink according to Eq. 2.8:

$$\frac{du_z}{dt} = \left(\frac{\rho_{em}}{\rho_p} - 1\right) g + \frac{3}{4}\frac{\rho_{em}}{\rho_p}\frac{C_D}{d_p}|u_{s\downarrow} - u_p|\left(u_{s\downarrow} - u_p\right) \tag{2.9}$$

where ρ_{em} and ρ_p are the densities of the emulsion at minimum fluidization and the large particle, respectively, and d_p is the particle diameter. The drag coefficient from the emulsion acting on the particle, C_D, can be expressed as:

$$C_D = \frac{8\tau}{\rho_{em}\left(|u_{s\downarrow} - u_p|\right)^2} \tag{2.10}$$

where τ is the shear stress, which was obtained from the dedicated experiments (discussed in more detail in Section 3.3).

Bubble wake zone
The large particle enters the bubble wake zone when it is trapped by a passing bubble, which occurs with a probability q for each bubble passage (*cf.* Ia and Ib in Figure 2.1). After fitting the model to the axial tracer distributions obtained from fluid-dynamically downscaled experiments, this work uses a constant q-value of 0.21 for this probability, as discussed in Section 3.2. Whether the tracked particle joins a bubble path within the same recirculation cell or in the closest neighboring cell is described by the sinusoidal probability curve shown in Figure 2.2.

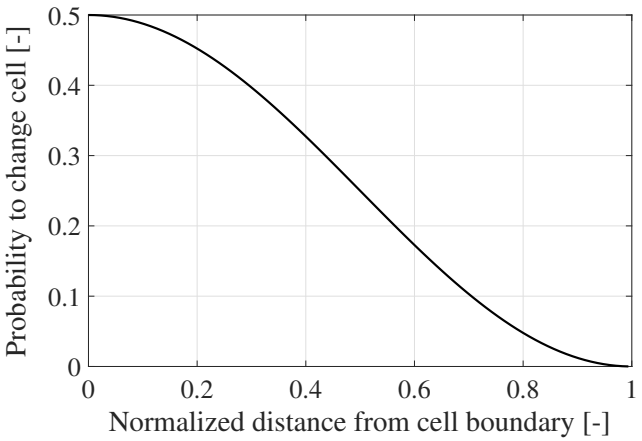

Figure 2.2: Probability of a tracked particle changing recirculation cell when joining a bubble wake.

As for the boundary conditions of the probability function, at the centre of the recirculation cell, the probability is zero, i.e., the particle will be dragged by a bubble rising in the same recirculation cell, while at the recirculation cell boundary there is a 50% probability to join a different cell.

Once the large particle has entered the bubble wake zone, it moves upwards with an average velocity that can be expressed as a fraction of the bubble velocity [71]:

$$u_p = \alpha \cdot u_b \tag{2.11}$$

The values of this ratio (here termed the *particle-to-bubble velocity ratio*), α, are discussed in Section 3.2, and lie in the range of 0.6–0.95. They are used by the model to reproduce hot conditions.

The probability that a particle will leave the bubble wake zone was evaluated with dedicated experiments and found to be very low. Therefore, this is not considered in the model. Instead, transfer back to the emulsion zone occurs exclusively through the splash zone.

Splash zone
When it reaches the dense bed surface, the particle is ejected into the splash zone by the erupting bubble. Experimental findings show that the motion of a large particle induced by the bubble eruptions follows a parabolic path [72]. The modulus of the ejection velocity of the particle, u_p, is a function of the bubble velocity at the bed surface, u_b, and the ejection angle, θ, as visualized in Figure 2.3.

$$u_p = u_b\Big|_{z=H_{bed}} \cdot cos(\theta) \tag{2.12}$$

The ejection angle, θ, follows a probability distribution given by the same experiments as:

$$P(\theta) = 0.046exp(-0.045\theta) \tag{2.13}$$

Furthermore, the model includes a scatter of the erupting bubble velocities in the form of a coefficient that follows a Gaussian distribution with a mean of 1 and a standard deviation of 0.32, as described previously [72]. With the vertical component of the ejection velocity and gravity as the only forces in the splash zone, the particle is assumed to follow a ballistic motion.

The ejection velocity and, thereby, the position of the ejected particle as it lands back on to the bed surface after its lateral displacement are determined by θ and the uniformly distributed ϕ, as shown in Figure 2.3. Both angles are also used to determine the position of a particle, which is changing zones inside the bed.

Once the particle completes its trajectory in the splash zone and lands on the bed surface, it rejoins the emulsion zone.

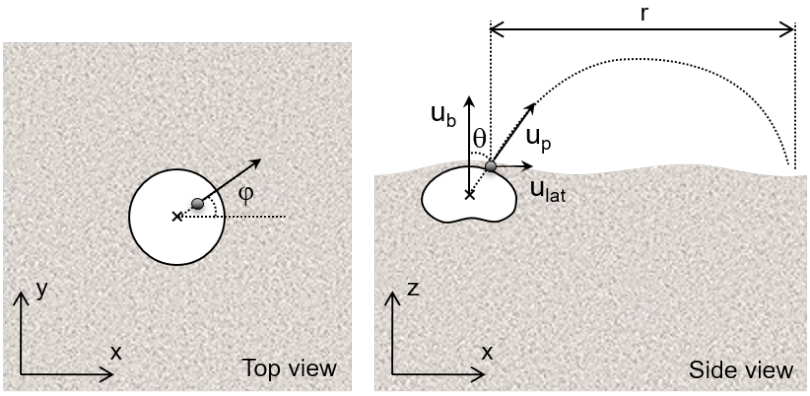

Figure 2.3: Angles assigned for lateral displacement of a particle in the bed or when released from an erupting bubble in the splash zone.

2.2 Model implementation

In the model, fuel mixing is simulated by continuously tracking the motion of a single, large particle as it follows the flow diagram in Figure 2.4, while governed by the expressions given in Section 2.1 for the three different fluid-dynamic zones illustrated in Figure 2.1. The particle trajectory is tracked with time-steps of $5e^{-3}$ s for a given simulation time, and the modeled trajectory data generated is used to extract the lateral dispersion coefficient (for, details, see Section 4.2). Note, that since only one particle is tracked, interactions between different fuel particles are not considered in the model.

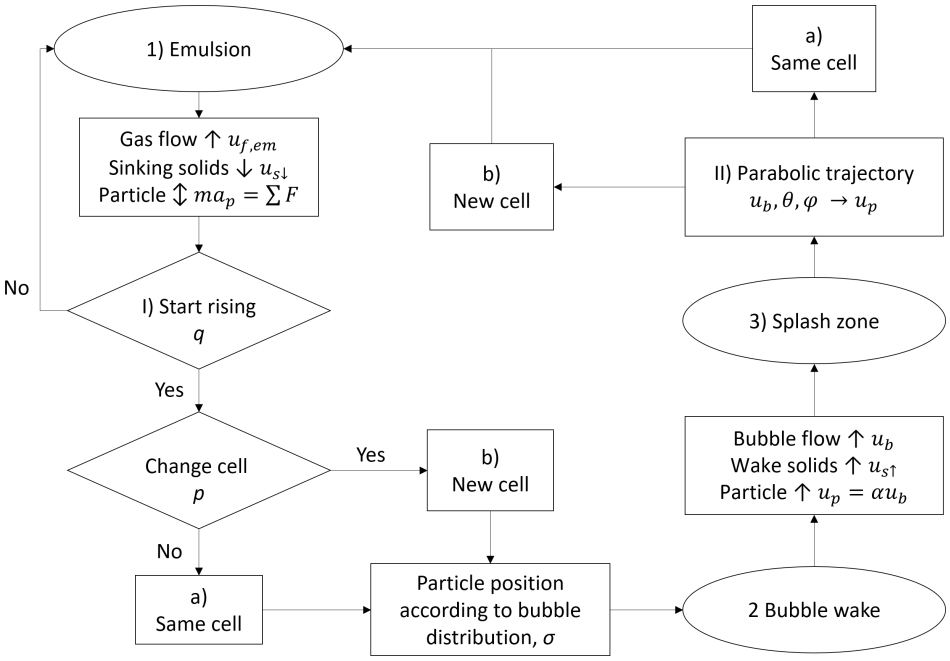

Figure 2.4: Computational flow diagram of the model used for tracking a large particle.

In line with the flow diagram given in Figure 2.4, the following assumptions are made: the fuel particle (over-bed feeding) starts at the top boundary (dense bed surface) of the emulsion zone, in which only axial displacement takes place. Subsequently, the particle is caught by a passing bubble and enters the bubble wake zone, where it follows the rising motion of the bubble. The action of entrapment by a passing bubble induces a lateral displacement, which may or may not represent a change of recirculation cell. When it reaches the bed surface the particle is ejected into the splash zone, where it follows a ballistic movement, eventually landing back onto the dense bed surface in the same cell or in a different recirculation cell, after which it rejoins the emulsion zone.

The input parameters to the model are the size and density of the modeled particle, the geometry of the reactor, and the operating conditions (bed height, fluidization velocity, bulk solids properties).

3 Experimental work

The experiments of this work were conducted to fill key knowledge gaps in the sub-models with relevant empirical content and to provide data for the validation of the overall mixing model (*cf.* left-hand and right-hand columns in Figure 1.5). This chapter introduces the experimental methods and setups, as well as the empirical content that results from the dedicated experiments and is used in the model formulation.

The principal measurement technique - used in all the experiments - was magnetic particle tracking, as presented in Section 3.1.

The parameters studied in the dedicated experiments, associated with the emulsion zone, the bubble wake zone and the transfer between the two zones, are depicted in Figure 3.1. In the bubble wake zone, the rising velocity of the large particle is expressed in terms of its ratio to the bubble velocity, u_b, denoted as α in this work. This particle-to-bubble velocity ratio, as well as the probability of the particle starting to rise (i.e., to change zone), q, were deduced from the experiments. The bubble wake fraction, f_w, was used as a fitting parameter after the values in the literature obtained from non-scaled cold units were shown to yield relatively weak axial mixing in comparison to measurements reproducing hot conditions.

The experiments dedicated to characterizing these mixing parameters are presented in Section 3.2 (**Papers III** and **IV**). The experiments were conducted applying fluid-dynamical downscaling (Section 3.2.1) to a bubbling bed (Section 3.2.2). The mixing parameters resulting from these experiments are presented in Section 3.2.3).

The effective drag force of the emulsion on large particles, F_D, which has been scarcely studied in literature, was further evaluated through dedicated experiments conducted in an incipient fluidized bed (see Section 3.3; **Papers V** and **VI**).

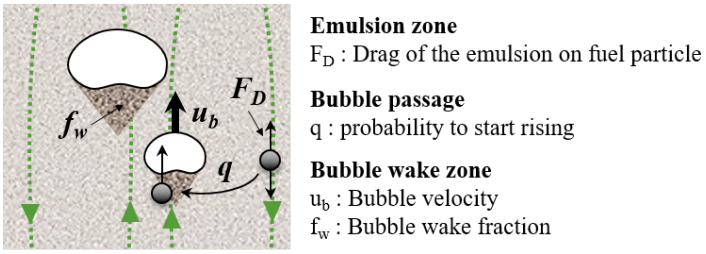

Figure 3.1: Key parameters of the mixing model to be studied with dedicated experiments.

Furthermore, fluid-dynamic downscaling was applied to provide data measured in cold units with quantitative relevance for hot industrial-scale conditions, as prerequisites for the validation of the model (**Papers I** and **IV**). The model validation is presented in Chapter 4.

3.1 Measurement techniques

3.1.1 Magnetic particle tracking

The most commonly used tracking methods used in FBs are optical tracking, X-ray tomography, magnetic resonance imaging (MRI) and radioactive (or positron emission) particle tracking methods (RPT, PEPT) [73]. Optical methods have been used under cold and hot conditions [74], although their use is limited to 2D beds [71, 75] or to examining the surface of the bed [34, 74]. Tomographic methods can be used to track bubbles [41] or particles [76, 77] in 3D laboratory-scale beds, and they have been deployed for temperatures of up to 400°C [78]. While MRI was previously limited to low temporal resolutions, it has recently been advanced to allow real-time tracking for investigating the fluidization dynamics of a laboratory-scale 3D bed [79]. RPT requires extensive safety precautions, but can be applied to follow several tracers with high accuracy and has been used in cold 3D beds by several groups [80–83]. However, continuous tracking of individual tracer particles in fluid-dynamically downscaled units is severely limited due to the use of metallic powders as bed materials, which are applied to fulfil the density ratio for the purpose of dynamic similarity (*cf.* Eq. 3.3).

In the last decade, magnetic particle tracking (MPT) has emerged as a technique that allows for 3D tracking with high spatial and temporal resolutions of the tracer trajectories [84, 85]. It has been applied to multiphase systems [86–88]. MPT comes with a number of benefits, e.g., both the position and orientation of the tracer particle can be measured in all three dimensions, providing better performance and wider scope than X-ray tomography, while it is relatively cheap and does not require extensive safety precautions [89, 90]. Experimental data obtained with MPT and reported in the literature are still scarce and limited to pseudo-2D beds or very narrow reactors and without any application of fluid-dynamical scaling laws, except in the case of an initial study carried out at Chalmers University of Technology [91], which used MPT to validate the applicability of fluid-dynamic scaling to the mixing of large particles in FBs.

All the tracking measurements in this work (**Papers I**, **III**–**VI**) were made with magnetic particle tracking, using a number of sensor assemblies to track a single tracer particle, which consisted of an NdFeB-based permanent magnet (see Figure 3.2). Each sensor assembly contains a three-axis Anisotropic Magneto Resistive (AMR) sensor, which is powered by an external voltage source and is located in the middle of the assembly (Figure 3.2a). The measured tracer positions have high spatial and temporal resolutions (±0.001m, 0.005 s) [91]. An example of the tracer trajectory in a FB is shown in Figure 3.2b.

The AMR sensor is manufactured with a default direction, which will change in response to an approaching magnetic field, thereby affecting the electrical resistance of the sensor. Five variables are unknown in this system: the position (x, y, z) and

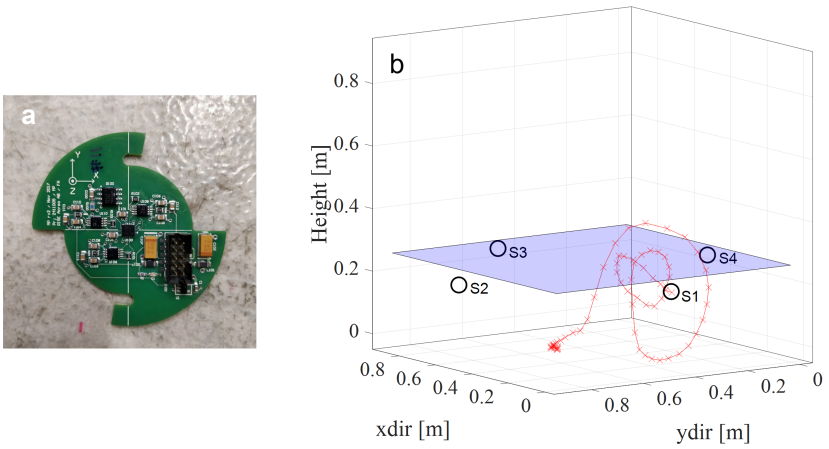

Figure 3.2: Magnetic particle tracking. a) Sensor assembly with AMR sensor located in the middle of the assembly. b) Resulting tracer trajectory from the fluid-dynamically downscaled FB. The four sensor assemblies, placed on each side wall of the squared bed, are indicated with the letter *S*. The initial bed height is indicated by the blue plane.

rotation (φ, θ) of the tracer. With four or five sets of the three-axis sensors, a total of 12 or 15 measurements is collected at each sampling point, resulting in an over-determined system, which is solved by minimizing the squared difference between the modeled and measured magnetic field. Noise that originates from magnetic fields surrounding the measurement device can be subtracted in the data analysis by taking a background measurement before each experiment.

The magnetic field range of the sensors is ±0.6 mT, which can be exceeded when the magnetic tracer is located too close to the sensing elements. Once saturated, the sensor can be restored with magnetization by sending two short electric pulses, so-called set/reset (S/R) pulses, to the sensor. As sensor saturation is not easily detectable, S/R was performed synchronously with the sampling frequency to ensure that all the sensor elements were measuring properly. However, with this procedure, the sampling frequency is restricted to around 20 Hz, as restoration of a sensing element by an S/R pulse requires a corresponding time. **Paper III** presents a solution to the sensor restoration issue based on enabling asynchronous S/R pulses while measuring, thereby yielding higher sampling frequencies (up to 200 Hz). Furthermore, a method to detect and remove data signals from saturated sensors was developed.

In **Paper IV**, tracers with stronger magnetic fields were used, such that the sensor elements were moved further away from the bed wall to minimize sensor saturation. As the magnetic fields of the tracers were stronger, this did not result in a reduction of the signal strength. In addition, the modeled magnetic field implemented in the code that solves the minimization problem was modified so as to allow for tracers with different magnetic strengths to be used.

In the **Papers V** and **VI**, a new generation of sensors was used, for which the S/R algorithm was enhanced by being performed consecutively. This means that the alternating S/R pulses are sent to one of the five sensors at a time, resulting in a maximum sampling frequency of 1.25 MHz/(3N), where N is the number of sensor elements. The measurement data are filtered with a median filter yielding a final sample rate of 5 ms. This frequency was shown to be required to resolve the tracer trajectory given the high tracer velocities occurring in the unit (for detailed analysis, see **Paper III**).

3.1.2 Pressure measurements

In this work, pressure measurements using differential pressure transmitters were conducted to determine the minimum fluidization velocities of various beds, the characteristic curve of the air distributors, and the bed voidage.

Table 3.1 gives the accuracy of the pressure transmitters used. Pressure measurements were acquired with a frequency of 10 Hz. The data points given in Figure 3.3 were obtained after averaging over the whole measurement time. The maximum standard deviations for each point are not plotted in the plots but were below 5%.

Table 3.1: Specifications of the pressure transmitters. Huba Control Type 664.

	Transmitter	Characteristic line	Total accuracy
Bed	20 mbar	±0.5 mbar	±1 mbar
Plenum	200 mbar	±0.5 mbar	±1 mbar

Figure 3.3a exemplifies the measurement of the minimum fluidization velocity, which is determined by the intersection of the line fitted to the decreasing pressure in the packed bed (gray dots) and the horizontal line of the pressure drop beyond the minimum fluidization (blue dots).

For the measurements in the fluid-dynamically downscaled bed, a total of four different perforated plates with varying pressure drop characteristics was used for the air distribution (Figure 3.3b). HP was a high-pressure drop plate with 5×5 1.5-mm holes. LP1, LP2 and LP3 were low-pressure drop plates with 9×9 1.1-mm, 7×7 1.4-mm and 5×5 2.6-mm holes, respectively, which mimicked the pressure drops typically used for the design of industrial units [46].

The emulsion density, ρ_{em}, plays an important role in the buoyancy and drag forces exerted on an immersed object and can be expressed as a function of the bed porosity [46], which in turn can be determined by measuring the pressure difference, Δp, along a distance, Δz, in the dense bed [67], which here is at minimum fluidization:

$$\rho_{em} = (1 - \varepsilon_{mf})\rho_s + \varepsilon_{mf}\rho_f \tag{3.1}$$

$$\frac{\Delta p}{g\Delta z} = (1 - \varepsilon_{mf})(\rho_s - \rho_f) + \varepsilon_{mf}\rho_f \tag{3.2}$$

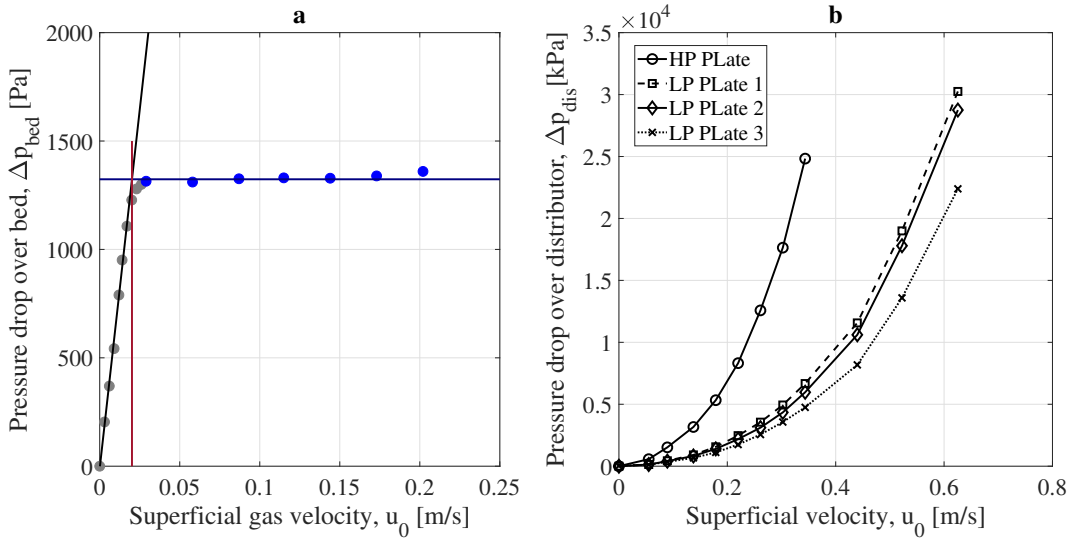

Figure 3.3: a) Pressure measurement to determine the minimum fluidization velocity (decreasing gas velocity in bronze powder). b) Pressure drop characterization of the perforated distributor plates used in the fluid-dynamically downscaled bed.

3.2 Mixing of large particles in bubbling fluidized beds

In order to provide both the model validation data and the experimental correlations applied by the semiempirical modeling with validity for hot industrial-scale conditions (*cf.* left-hand and right-hand columns in Figure 1.5), mixing measurements were are carried out in a fluid-dynamically downscaled FB unit operated under bubbling conditions, to which magnetic particle tracking was applied.

3.2.1 Experimental method

Fluid-dynamic scaling is a method that allows one to mimic the fluid-dynamics under industrial conditions (i.e., large-scale, high temperatures) in a smaller unit operated under ambient conditions. Scaling facilitates the exploitation of diagnostic techniques that are unsuitable for hot conditions and enables operational and geometrical flexibilities in a safer and cheaper environment than that of industrial units.

Fluid-dynamic scaling is achieved by applying a set of dimensionless parameters to fulfil the geometric and dynamic similarities of a scaled model to its matching industrial unit. With application to FBs, such sets were formulated by Glicksman et al. [92] and Horio et al. [93] and validated by several authors as being suitable for investigations, for example, of hydrodynamics and mixing [94–96]. The scaled model

in this work applies the full set of scaling parameters as proposed by Glicksman [97], which consists of the Froude number, the solids-to-gas density ratio, the particle Reynolds number, the fluid Reynolds number, the scaled solids circulation flux, the bed geometry, and the particle size distribution, reading as follows:

$$\frac{u_0^2}{gL}, \frac{\rho_s}{\rho_f}, \frac{\rho_s u_0 d_s}{\mu_f}, \frac{\rho_f u_0 L}{\mu_f}, \frac{G_s}{\rho_s u_0}, \frac{L}{d}, \phi, PSD. \tag{3.3}$$

Here, the experimental work is carried out in a unit without any forced solids circulation. Thus, the parameter related to the solids circulation flux is disregarded. Instead, the pressure drops over the air distributor and over the bed height are considered.

3.2.2 Experimental setup

The unit used for sampling the experimental data in **Papers III** and **IV** (with the data also being used for the model validation in **Paper I**) was a bubbling bed with a square cross-section of 0.17×0.17 m^2, as shown in Figure 3.4.

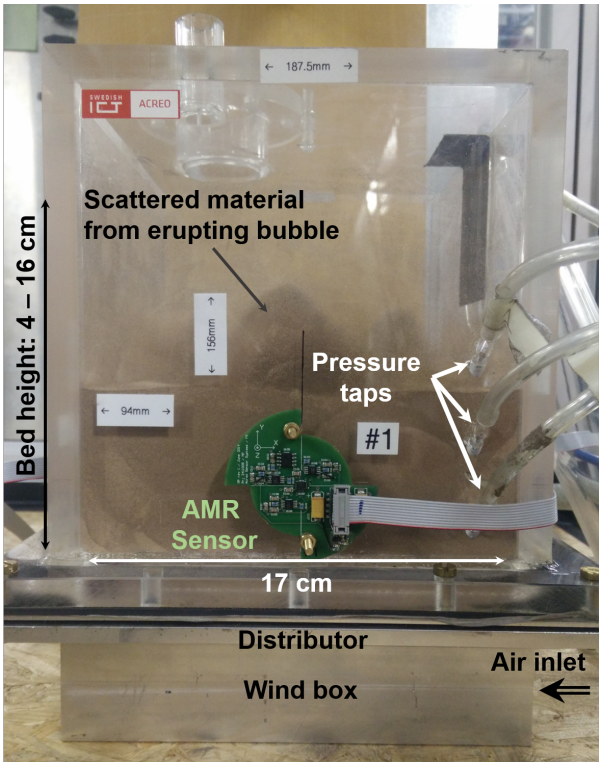

Figure 3.4: Experimental setup. Fluid-dynamically downscaled bubbling bed with bronze powder. One AMR sensor can be seen in the foreground.

The bed consisted of bronze powder with a mean particle diameter of 60 µm and a solid density of 8900 kg/m^3, fluidized with pressurized air at ambient temperature with one (out of four available) perforated distributor plate (Figure 3.3b). This

yielded scaling factors of 4.4 and 5.0 when upscaled to air at 800 °C and 900 °C, respectively. The bed was equipped with one pressure tap at the air inlet and three taps inside the bed. The tracer trajectory was measured with a set of four MPT sensor assemblies, which were placed on each side wall at a height of 45 mm.

Table 3.2 summarizes the different scaling sets applied in **Papers I**, **III** and **IV**, and the input parameters used for each setup. **Paper III** used a cylindrical tracer (d_p=0.03 m, H=0.015 m) with a fixed density of 1890 kg/m^3, designed to resemble an anthracite particle under air combustion at 900°C, which resulted in a length scale factor of 5. All four distributor plates were used in this work (see Figure 3.3b).

With further development of the MPT method using encapsulated spherical tracers of constant size (d: 0.04 m) but of variable densities, the measurements in **Paper IV** reproduced different fuel particles in air combustion at 800°C. The three different tracer densities were chosen to represent two typical biomass fuels, namely biochar (400 kg/m^3) and fresh biomass (810 kg/m^3), as well as a neutrally buoyant tracer (1180 kg/m^3). In this work, two of the four distributor plates (HP and LP2; see Figure 3.3b) were used. The data in **Paper IV**, which were obtained with the LP2 distributor plate, include measurements made with two additional tracer sizes (i.e., as well as 0.04 m, we used 0.08 m, and 0.12 m), and these were used for validation of the axial model in **Paper I**.

Table 3.2: Scaling parameters used in the experiments in **Papers I**, **III** and **IV**. Upscaled values represent hot conditions (combustion).

	Downscaled	Upscaled (**Paper III**)	Upscaled (**Papers I+IV**)
Temperature,°C	20	900	800
Length scaling, -	L	$5.0L$	$4.4L$
Mass scaling, -	m	$29.7m$	$22.7m$
Time scaling, -	t	$2.2t$	$2.1t$
Bed dimensions, m	0.17×0.17	0.85×0.85	0.74×0.74
Bulk solids size, µm	60	300	250
Bulk solids density, kg/m^3	8900	2600	2600
Min. fluid velocity, m/s	0.03	0.07	0.06
Fixed bed height, m	0.03 - 0.07	0.15; 0.25; 0.35	0.18; 0.30
Fluidization velocity, m/s	0.01 - 0.5	0.07 – 0.43	0.013 – 0.528
Tracer size, m	0.003 - 0.03	0.03, 0.015	0.04; 0.08; 0.12
Tracer density, kg/m^3	1470 - 7310	1890	350; 800; 1230

For all the experiments carried out in the fluid-dynamically downscaled bed, the magnetic tracer was dropped into the bed from above. The initial measurement time was set to 60 min. However, the results in **Paper III** confirmed that a measurement

time longer than 15 min did not yield additional information in terms of axial and lateral mixing. Thus, a test duration of 15 min was set to avoid significant loss of the bed material through elutriation.

3.2.3 Mixing parameters derived from experiments

From the above described experiments, the mixing parameters (α, q, f_w, as presented in Figure 3.1) were investigated.

Particle-to-bubble velocity ratio
Previous studies have estimated the rising velocity of large particles in FBs to be in the range of 10%-30% of the bubble velocity [48, 71, 75, 80, 98]. This spread in the literature values is mainly attributed to the wide variety of units (pseudo-2D and 3D, of various sizes), solids, and operational conditions applied, although it must be noted that all their measurements were conducted under cold non-scaled conditions.

This work found that the rising average velocity of the tracer particle on a hot upscaled basis was much higher than the values cited in the literature, as shown in Figure 3.5.

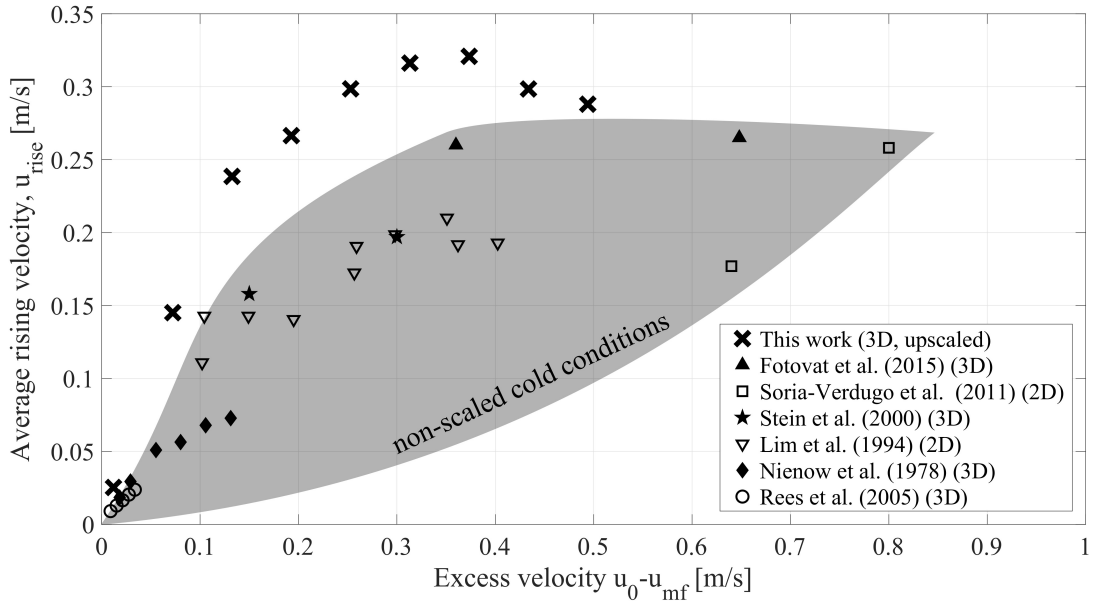

Figure 3.5: Average tracer rising velocity in the dense bed, u_{rise}, vs. excess gas velocity, $u_0 - u_{mf}$. In this work, the bed height was 0.3 m, compared to the data from the literature covering bed heights in the range of 0.15-0.5 m and bed solid densities in the range of 1100-2940 kg/m^3. Neutrally buoyant tracer.

The literature data cover bed heights of 0.15-0.5 m, bed material solid densities and diameters of 1100-2940 kg/m^3 and 212-800 µm, respectively, and apply neutrally buoyant tracers. Nienow et al. [48] and Rees et al. [98] have used the rather simple measurement method of releasing the tracer close to the distributor in 3D beds and observing the time that it takes for the tracer to reach the bed surface. Soria-Verdugo

et al. [71] and Lim et al. [75] have measured with optical tracking methods in 2D units, while Fotovat et al. [82] and Stein et al. [81] have used radioactive particle tracking methods. The studies that applied particle tracking methods, including this work, have presented tracer particle velocities that are averaged over the dense bed height.

Figure 3.5 shows that the rising velocities increase with fluidization velocity and level out at an excess velocity of around 0.3 m/s. Data from non-scaled cold units described in the literature follow a similar qualitative trend but yield generally lower values. Although the bubble velocity is a function of the bed material properties, bed height, and fluidization velocity, and therefore differs between the data series given in Figure 3.5, the much higher α-values obtained in the present work indicate an impact of the scaling (temperature) effect.

A similar observation of increased mixing of larger solids with temperature was earlier reported for the lateral mixing. Thus, Olsson et al. [34], using an industrial-scale unit operated under cold conditions, experimentally derived a lateral fuel dispersion coefficient that was less than half that obtained by Sette et al. [96] using a scaled model resembling hot conditions in the same unit. Yet, the work of Sette et al. [96] was validated using a scaled model to replicate successfully the experimental work of Niklasson et al. [99], who operated another industrial-scale unit under hot conditions. This comparison shows that the smaller (and thereby slower) bubbles generated under cold conditions induce less-intense solids mixing than the larger and faster bubbles generated under hot conditions, which can be mimicked through the application of fluid-dynamical scaling.

With this, the particle-to-bubble-ratio to be used in the semiempirical model (α=0.6) could be obtained from the measured rising velocities and the bubble velocity, u_b, as calculated with Eq. 2.2 in Chapter 2, with both averaged over the bed height (Figure 3.6).

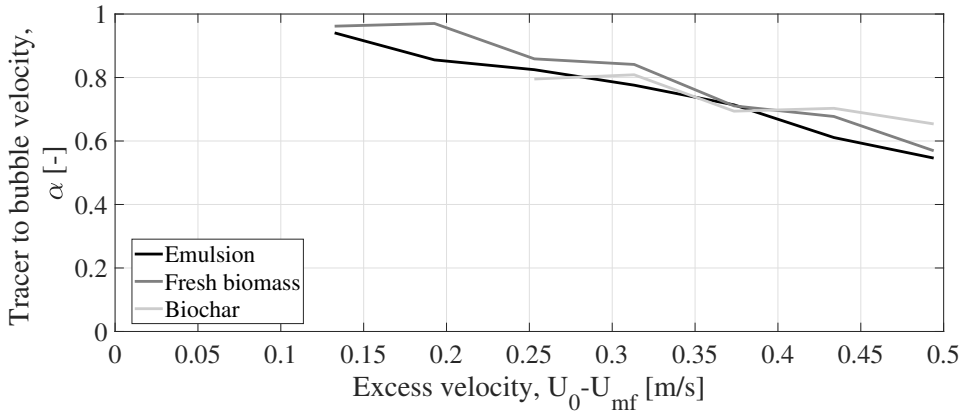

Figure 3.6: Particle-to-bubble velocity ratio, α, vs. excess gas velocity, $u_0 - u_{mf}$. Tracer velocities are from measured data (d_p = 0.04 m, ρ_p = [400;810;1180] kg/m^3) and bubble velocities are calculated with Eq. 2.2, with both averaged over the bed height.

For the studied conditions, comparison of three different tracer densities showed that α is relatively independent of the tracer density but decreases (from about 0.94 to 0.55) with excess velocity.

Bubble wake fraction
The bubble wake fraction, f_w, which describes the amount of solids being dragged upwards in the bubble wake zone (*cf.* Figure 3.1), needs to be quantified in order to calculate the sinking bulks solids velocity in the emulsion zone from the mass balance of rising and sinking solids (*cf.* Eq. 2.8). Using a bubble wake fraction from the literature for similar bulk properties but measured under cold conditions [39] yielded poor axial mixing of the large particle when modeling the experimental data obtained in the fluid-dynamically downscaled bed from this work. A fitted value of $f_w = 0.63$ was, therefore, obtained by minimizing the squared error between the measured and modeled axial distributions of the tracer. This fitting has been carried out previously and with data other than those used for the validation of the 3D model, as presented in Section 4.1.

Figure 3.7 depicts the influence of the bubble wake fraction on the modeled probability density function of the vertical location of a biochar particle and a fresh biomass particle at low and high superficial gas velocities, respectively.

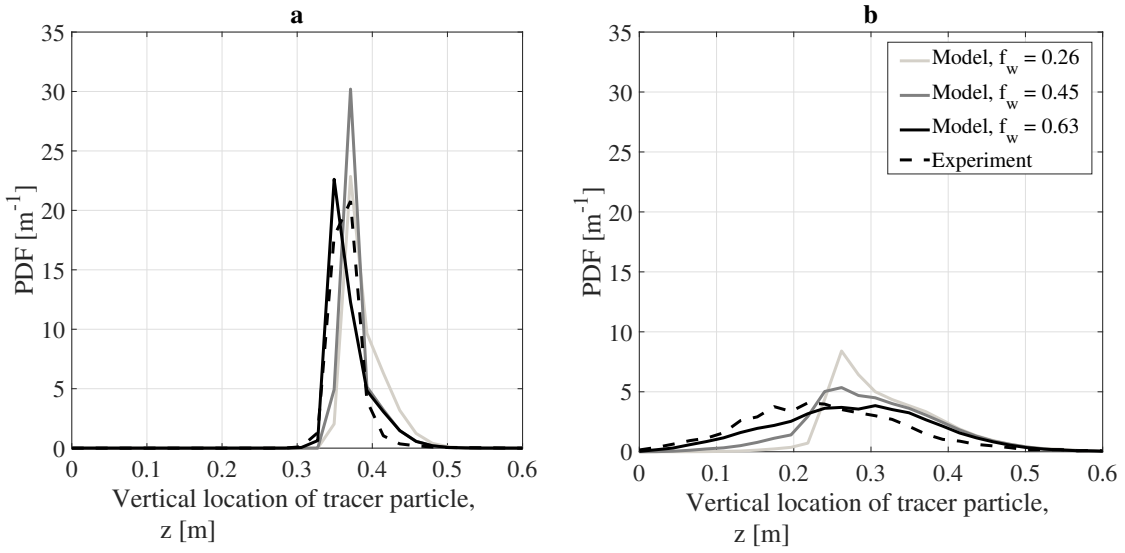

Figure 3.7: Modeled and experimental probability density function of the vertical location of a fuel particle. a) Biochar, $d_p = 0.04$ m, $\rho_p = 400$ kg/m^3, $u_0 = 0.18$ m/s. b) Fresh biomass, $d_p = 0.04$ m, $\rho_p = 810$ kg/m^3, $u_0 = 0.48$ m/s. $H_0 = 0.3$ m.

An increasing bubble wake fraction mainly improves the mixing into the bed of the heavier fresh biomass particle at higher velocities. This is because with increasing downwards velocities of the solids emulsion zone the denser particle is more easily dragged into the bed.

Probability to start rising

In the model, the probability of the large particle joining the bubble path and starting to rise enables the circulation of the particle between the different zones. This probability, q, was investigated in the experiments with the fluid-dynamically downscaled bed for several tracer densities and diameters

Figure 3.8 shows the probability (per bubble passage) for a spherical tracer (d_p = 0.04 m, $\rho_p = 1180$ kg/m^3; neutrally buoyant) to start rising in the bed. The fixed bed height was 0.3 m and the fluidization velocities ranged from 0.12 m/s to 0.54 m/s. The probability that the particle will transfer into the bubble wake zone is highest close to the bottom of the bed and decreases gradually with increasing height in the bed. Increasing the fluidization velocity increases this probability as the bubbles grow bigger, making it more likely that they will drag along the tracer particle.

The influences of tracer size and density have also been investigated, although no clear trend for lighter and/or bigger particles was observed. It should be noted the flotsam behaviors of some tracers make it difficult to gather measurement points inside the dense bed for those cases in which buoyancy forces predominate.

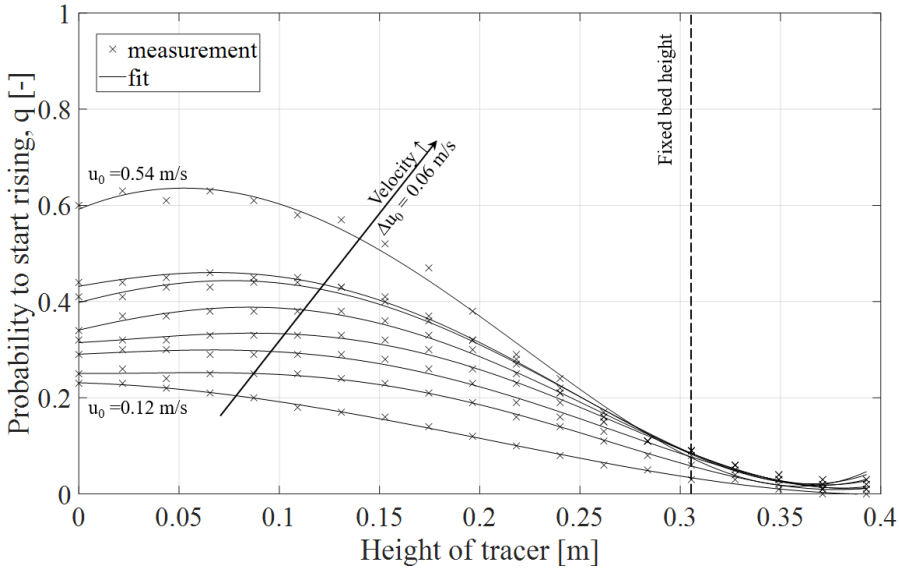

Figure 3.8: Probabilities to transfer from the sinking emulsion to the bubble wake solids zone, q. Tracer particle: $d_p = 0.04$ m, $\rho_p = 1180$ kg/m^3, $H_0 = 0.3$ m, $u_0 = 0.06 - 0.54$ m/s.

Although the probability to start rising varied significantly with height and fluidization velocity, it showed very little impact on the results of the axial model. Thus, no significant difference in the modeled results was observed when using the height-resolved probability curves corresponding to each case, constant (height-averaged) probability values corresponding to each case or the same constant probability value for all the cases. Given this low-level sensitivity, a constant value with height of q=0.21 was applied to all the modeled cases.

3.3 Drag on large particles in incipient fluidized beds

The experiments performed in the incipient fluidized beds aim at enabling the modeling of the motion of the large particle in the emulsion zone, based on the equation of motion (see Eq. 2.9), i.e., the left-hand column as presented in Figure 1.5. This requires knowledge of the drag force exerted by the bulk solids emulsion at minimum fluidization on the immersed particle, which is a major contributor to the motion of the particle . The results can be found in **Papers V** and **VI**.

3.3.1 Experimental method

In general terms, the drag force is dependent upon the density of the fluid, the projected area of the particle, and the slip velocity, i.e., the relative velocity of the particle to the fluid. The general definition reads:

$$F_D = \frac{\pi}{8} d_p^2 C_D \rho_f |u_f - u_p|^2 \tag{3.4}$$

The drag coefficient, C_D, varies with the slip velocity, the size of the particle and the resistance of the fluid to deform or flow. In Newtonian fluids, this resistance is called the *viscosity* and is defined as the ratio of the shear stress, τ, to the shear rate, $\dot{\gamma}$, i.e., the shear stress reads:

$$\tau = \mu_{eff} \cdot \dot{\gamma}. \tag{3.5}$$

Applied to this work, the *fluid* of interest is the bulk solids emulsion at minimum fluidization (see Eq. 2.1, i.e., a dense gas-solids suspension, the viscosity of which is unknown.

Particle suspensions typically exhibit non-Newtonian behavior with fluid properties that vary according to the shear rate [60], i.e., they do not exhibit a constant viscosity and their description requires more complex models as, for example, the Herschel-Bulkley model [100], in which the shear stress is expressed as:

$$\begin{aligned} \tau &= \tau_0 + k \cdot \dot{\gamma}^n & \tau &> \tau_0 \\ \dot{\gamma} &= 0 & \tau &< \tau_0 \end{aligned} \tag{3.6}$$

where k is the consistency index, which gives an indication of the resistance of the fluid to flow, n is the flow-index, which gives an indication of how fast the resistance to flow changes with shear rate, and τ_0 is the so-called *yield stress*, an initial stress, which must be exceeded for the fluid to flow. For $n < 1$ the fluid exhibits a shear-thinning behavior, whereas for $n > 1$ the fluid is shear-thickening. For $n = 1$ and $\tau_0 = 0$ the fluid is Newtonian, whereas for $\tau_0 > 0$ the fluid is deemed to be *Bingham plastic*. Shear-thinning fluids ($n < 1$) that exhibit a yield stress ($\tau_0 > 0$) are termed *viscoplastic*.

The rheological behaviors of gas-fluidized beds have been discussed in the literature for decades, with groups reporting different fluid flow behaviors, including Newtonian [98, 101–104], Bingham plastic [105], shear-thinning [106–108]. As the high concentration of solids with dominating particle-particle interactions and the intrinsic instability of gas-solid FBs make prediction of an apparent viscosity through models challenging, experimental investigations are widely used.

There are two main experimental methods described in the literature: rotational viscometers [105,106,108,109], and the falling sphere method [98,101–104] (Table 3.3).

While for FBs, experiments with the falling sphere method have been mainly limited to poorly resolved trajectories using a Newtonian approach to obtain the emulsion viscosity under assumed terminal conditions, experiments with rotational viscometers have confirmed the non-Newtonian behaviors of FBs, as suggested by Grace [107]. Rotational viscometers allow full control over the applied share rates, which enables well-resolved stable measurement conditions. However, these viscometers cannot measure the interaction of the bed with an immersed particle and are unable to apply low shear rates, which makes them unsuitable for measuring a potential yield stress.

Chhabra [110] has discussed the applicability of the falling sphere method to non-Newtonian fluids, which has less control over shear stresses and rates and is limited due to the non-uniformity of both the shear stress and the shear rate in these so-called *non-viscous* fluids. However, by combining the falling sphere method with a well-resolved tracking technique (such as MPT), it is possible to evaluate some characteristics of non-viscous fluids. For example, the interaction of the immersed particle with the fluid and, by applying different sizes and densities of spheres, the behaviors at low shear rates and when stagnating, i.e., the zero-shear stress or yield stress, can be evaluated.

The objective of this part of the work was to understand the effect of the rheological behavior of the emulsion on immersed particles, so as to deduce a correlation for the effective drag force that can be used to model the fuel motion. For this, the falling sphere method was used, based on the release of different spherical tracers with defined sizes and densities into incipient fluidized beds.

The characteristic shear rate, $\frac{u_{rel}}{d_p}$, is taken as the ratio of the relative tracer-to-fluid flow velocity to the tracer diameter. The motion of a tracer moving vertically in the bed induces a vertical flow of the bed solids, which adopt a velocity according to the continuity equation:

$$u_{em} = \frac{d_p^2}{(d_b^2 - d_p^2)} u_p = \lambda u_p. \tag{3.7}$$

The shear stress is defined as the drag force exerted over the surface area of the tracer. For non-Newtonian fluids, one may expect both the shear stress and shear rate to vary from point to point over the surface of the tracer [110], and there are different suggestions in literature as to whether to use the whole or parts of the surface area

Table 3.3: Rheometric methods commonly used in FBs.

Method		Positive aspects	Negative aspects	Literature
Rotational viscometer	Rotational body in the fluid, apply different rotational speeds (shear rates), measure torque (shear stress.) on the body, gives intrinsic viscosity.	Full control over shear rates enables stable measurement conditions.	Not able to measure interaction with immersed particle, only high shear rates can be applied.	Schügerl et al. (1961) [106]: Shear-thinning fluid, Newtonian for low shear stress. Anjaneyulu and Khakhar (1995) [105]: Bingham fluid. Colafigli et al. (2009) [108]: Shear-thinning fluid. Lv et al. (2018) [109]: Newtonian fluid.
Falling sphere method	Release of spherical bodies into fluid, measuring terminal velocity, calculate drag and Re gives the eff. viscosity on the immersed body.	Able to catch influence of the falling particle, zero-shear stress can be reached by varying size and density of spheres.	Interaction with falling body, low controllability over the experiment, meaning of eff. viscosity is unclear for non-Newtonian fluids.	Daniels (1959) [101]: Newtonian fluid. King et al. (1981) [102]: Newtonian fluid. Kai et al. (1991) [103]: Newtonian fluid. Rees et al. (2005,2007) [98, 104]: Newtonian fluid, incl. defluidized hood.

when calculating the shear stress. Andres [111] has derived a definition of the drag force using only the vertical projection of the shear stress over the sphere surface, while Uhlherr and colleagues [112] have used the definition of the Stokes flow in a Newtonian fluid. This work uses the averaged shear stress over the total surface area of the sphere, similar to the work of Hirota and Takada [113].

Solving the equation of motion (Eq. 2.9) in the vertical dimension for a spherical tracer, the shear stress can be expressed as:

$$\tau = \frac{F_D}{A_s} = \frac{1}{8} C_D \rho_{em} (1-\lambda)^2 u_z^2 = \frac{1}{6} d_p \Bigg(\underbrace{g\left(\rho_{em} - \rho_p\right)}_{\text{buoyancy}} + \underbrace{\frac{du_z}{dt}\rho_p}_{\text{acceleration}} \Bigg). \tag{3.8}$$

For fluids that exhibit a yield stress, a common way to study the relationship between stress forces and gravitational forces is to normalize the shear stress according to the tracer buoyancy, removing the dependency on the sphere properties, such that:

$$Y = \frac{\tau}{g d_p (\rho_{em} - \rho_p)}. \tag{3.9}$$

For decreasing shear rates, the normalized shear stress, Y, approaches $\frac{1}{6}$, which is at zero shear rate called the *yield gravity parameter*, Y_0. This parameter is a static equilibrium of the sphere in a viscoplastic media [110], i.e., a normalized shear stress fluctuating around Y_0 indicates prevalence of the yield stress, data-points above Y_0 indicate a dominant stress effect, while data-points below Y_0 suggest a dominant net gravitational effect.

3.3.2 Experimental setup

The falling sphere method was exploited in several experiments using various bed materials that were fluidized to their minimum fluidization velocities under atmospheric pressure with ambient air in a cylindrical bed (0.074 m i.d.), while different falling and rising tracers were released into the bed. The bed was fluidized using a porous distributor plate to ensure a high pressure drop and achieve homogeneous distribution of the flow, i.e., stable fluidization for operation at the minimum fluidization velocity. The unit was equipped with five MPT sensor assemblies (placed on the four side walls at three different heights), which were used to measure the trajectories of the freely moving tracers, as depicted in Figure 3.9.

The concept was developed through an initial group of experiments, using a bed of glass beads with a narrow size range (212-250 µm, 2486 kg/m^3). Furthermore, a systematic selection of Geldart Group B bulk materials was carried out for the purpose of varying the particle size, density and sphericity. This was done to extend the understanding of the dependence of the momentum exchange between gas-solid

suspensions and immersed spheres on varying bulk solids properties. The various materials are summarized in Table 3.4.

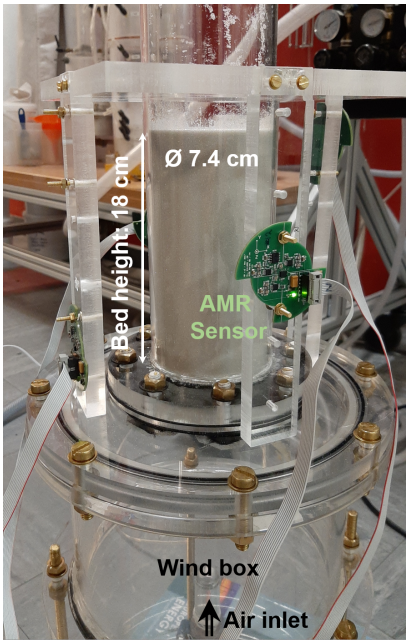

Figure 3.9: Experimental setup of the incipient fluidized bed (here, with glass beads).

Considering these characteristics, four different comparisons were proposed to investigate the impact of each of the three selected properties (see *Variation* in Table 3.4). The bed materials were also characterized regarding their angle of repose and bed expansion (from a settled bed to voidage under minimum fluidization conditions), to understand the effects of internal friction, flowability, and the density of the suspension.

With the aim to obtain a wide range of shear stresses and rates, a total of 12 spherical tracers, with four different diameters (5, 8, 10 and 20 mm) and various densities (negatively buoyant and positively buoyant), was chosen. Table 3.4 compiles the main tracer characteristics, including the buoyant densities (which depend on the bed in which they are immersed). Tracers with densities lower than the emulsion density are released from the bottom of the bed, from where they exhibit a rising trajectory (indicated with a + in the table). All other tracers are released from the bed surface, from where they sink into the bed (indicated with a - in the table). The minimum fluidization velocity of each bulk material was experimentally measured following the procedure described in Section 3.1.2.

Depending on the tracer density in relation to the emulsion density, the tracers would either fall or rise through the bed (Table 3.4), thus, the experiments were performed according to one of the following procedures:

Table 3.4: Properties of bed material and tracers of the experiments with incipient fluidized beds. Tracer behavior: rising (+); falling stagnating (−); falling non-stagnating (−)

	Glass beads	Glass beads	Glass beads	Glass beads	Bronze	Sand	Glass beads	Alumina	Sand
Particle size, µm	212-250	250-300	150-180	125-150	75-125	125-150	75-125	75-125	75-125
Density, kg/m^3	2486	2486	2486	2486	8471	2655	2486	1540	2655
Sphericity, -	1	1	1	1	1	0,75	1	0,85	0,75
Angle of repose, °	26.64	25.98	26.48	27.4	23.88	35.35	29.51	29.22	36.07
Bulk density, kg/m^3	1589	1450	1442	1446	5141	1397	1426	921	1370
Density at u_{mf}, kg/m^3	1465	1465	1346	1324	5144	1346	1346	847	1349
u_{mf}, m/s	0.0604	0.0604	0.0170	0.0123	0.0257	0.0170	0.0075	0.0045	0.0128
Δp at u_{mf}, mbar	31	31	23	21	75	23	21	13	22
Variation	-	d_s	d_s	d_s, ϕ	ρ_s	ϕ	d_s, ρ_s, ϕ	ρ_s	ϕ

Tracer	Size m	Mass g	Density kg/m^3	Net density in bed (weight – buoyancy) kg/m^3								
5_1	0.0050	0.490	7487	-5898	-6022	-6141	-6162	-2342	-6141	-6141	-6639	-6137
8_1	0.0080	2.030	7572	-5984	-	-6226	-6248	-2428	-6226	-6226	-6725	-6223
10_1	0.0100	4.030	7697	-6108	-6232	-6351	-6372	-2552	-6351	-6351	-6849	-6347
10_4	0.0100	2.320	4431	-2842	-2966	-3085	-3106	-	-3085	-3085	-3584	-3081
10_5	0.0100	1.600	3056	-1467	-1591	-1710	-1731	+2089	-1710	-1710	-2208	-1706
20_1	0.0200	32.050	7651	-6063	-6187	-6305	-6327	-2507	-6305	-6305	-6804	-6302
20_2	0.0205	28.890	6405	-4816	-4940	-5059	-5080	-1260	-5059	-5059	-5557	-5055
20_3	0.0200	20.340	4856	-3267	-3391	-3510	-3531	-	-3510	-3373	-3871	-3369
20_4	0.0200	17.470	4171	-2582	-2706	-2825	-2846	+974	-2825	-2825	-3323	-2821
20_5	0.0200	13.370	3192	-1603	-1727	-1846	-1867	+1953	-1846	-1846	-2345	-1842
20_6	0.0200	6.100	1456	-	+8	-110	-132	+3688	-110	-110	-609	-107
20_9	0.0200	1.270	303	+1193	+1161	+1043	+928	+4748	+950	-	+451	+953

- For falling tracers: after vigorous fluidization for a period of 60 s, the fluidization velocity was slowly decreased and set to the corresponding u_{mf}. The tracer was held right above the bed surface and released while the trajectory was recorded.

- For rising tracers: the tracer was held at the bottom of the bed with the help of a thin wire while the bed was fluidized. After 60 s of vigorous fluidization, the fluidization velocity was slowly decreased and set to the corresponding u_{mf}. The gas flow was momentary stopped (2 s) to remove the wire, and then restarted to allow the free rising of the tracer while the trajectory was recorded.

For each tracer and bed, a minimum of 10 repetitions was carried out, acquiring the tracer trajectories from MPT at a sampling rate of 200 Hz. The trajectories were filtered by applying three times a moving average with a window width of 8 points (i.e., 40 ms), to remove detection noise. The filtered position and time data were then used to calculate the velocity and acceleration of the tracer particle.

3.3.3 Shear stress derived from experiments

Three types of tracer trajectories were observed: 1) the tracer rises from the bottom to the surface of the bed; 2) the tracer falls from the surface but stagnates inside the bed; or 3) the tracer falls from the surface all the way to the bottom of the bed. Figure 3.10 gives examples of these three behaviors and how the trajectory data are edited to discard those parts for which the tracer is not fully immersed or its trajectory is affected by the bottom grid. The different behaviors of each tracer in each bed are indicated in Table 3.4 using the same color coding as in Figure 3.10.

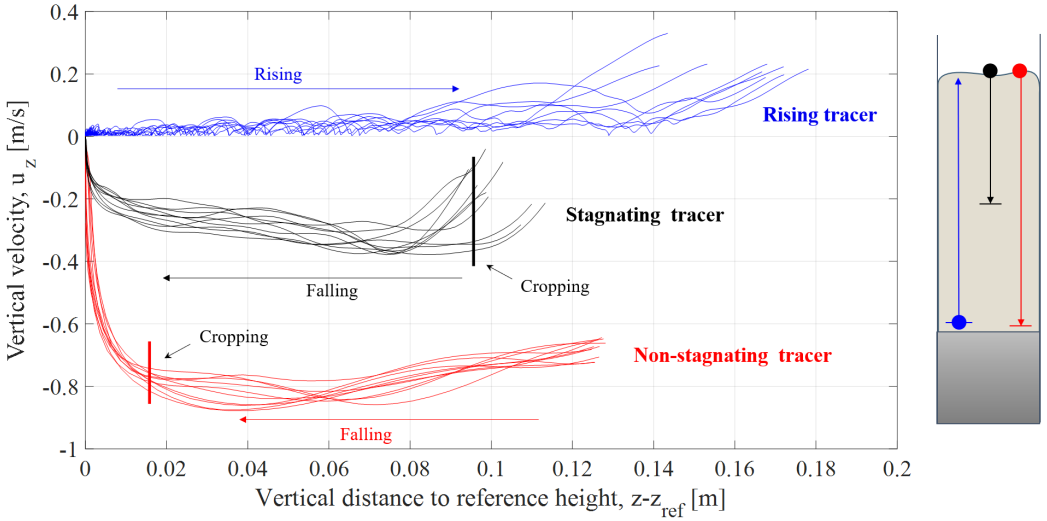

Figure 3.10: Vertical tracer velocity profiles vs. reference height for the three behaviors identified from the experiments: rising, falling stagnating, and falling non-stagnating. The height is given in relation to a reference height (horizontal line in the schematic), which is the starting point of the tracer, the stagnating height or close to the bottom of the distributor, respectively. The direction of the trajectory and data editing are indicated.

It should be noted that the repeatability of the trajectories is very high. Although the bed is fluidized vigorously and reset to u_{mf} after each measurement, the tracers follow similar trajectories for all ten repetitions.

With the velocity and acceleration of the particle, the shear stress, τ, and the normalized shear stress, Y, can be calculated with Eqs. 3.8 and 3.9, respectively. Rheograms plotting these values against the characteristic shear rate are discussed below for each of the behaviors separately.

Figure 3.11 shows the rheograms for a non-stagnating (fully immersed) tracer (20_5) in four different beds of glass beads with: a) shear stress vs. the shear rate; and b) normalized shear stress vs. shear rate. Non-stagnating tracers causes fluctuation of a certain shear stress for a range of shear rates as they fall with terminal velocity. When normalized, the shear stress fluctuates around the yield gravity parameter, Y_0, generating concentrated data around a dynamic equilibrium. These cases are evaluated by calculating the center of mass and standard deviation in both axes of the data cloud, as depicted in Figure 3.11a. From the center of mass an effective viscosity is calculated by dividing the mean shear stress by the mean shear rate (horizontal and vertical dashed lines in the figure). For this calculation the number of repetitions needed to obtain a stable value of the viscosity was calculated, which showed that after only 3 repetitions the variation in the values was less than 5%.

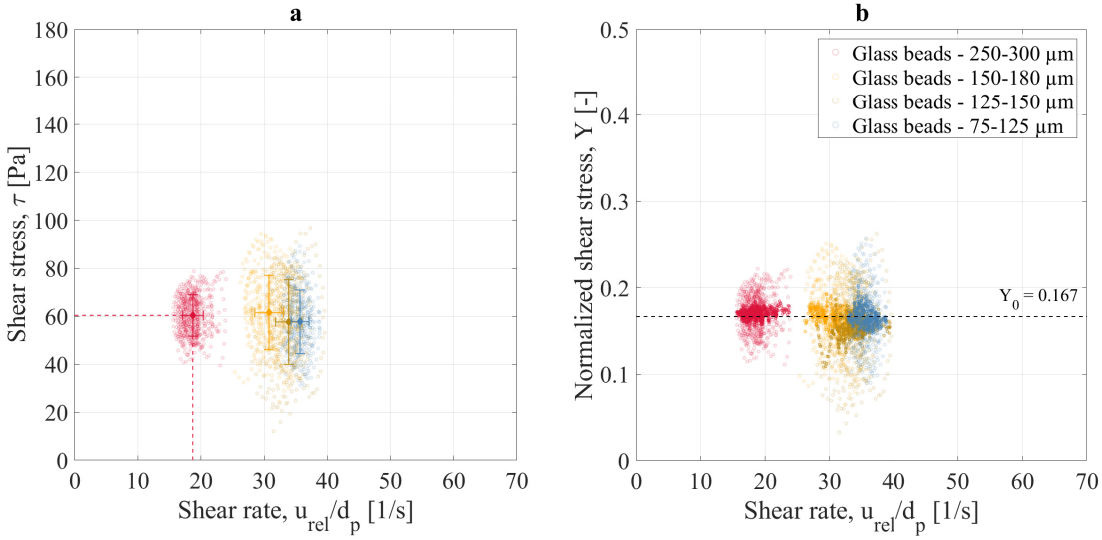

Figure 3.11: Relationship of the shear stress to the shear rate of a non-stagnating tracer (20_5) in four incipient fluidized beds of glass beads with varying solids size. a) Shear stress vs. shear rate. b) Normalized shear stress vs. shear rate.

Figure 3.12 shows the relationship of the shear stress to the shear rate of a stagnating tracer (10_4) in five different beds of glass beads with: a) the shear stress vs. the shear rate and b) the normalized shear stress vs. shear rate. Similar to the

non-stagnating tracer, the stagnating tracers form concentrated data around the dynamic equilibrium for a range of shear rates. However, the equilibrium appears to be disrupted as the tracer stagnates, as evidenced by a sudden increase in the shear stress ($Y > Y_0$), which ends in a new equilibrium point at zero shear rate and Y_0, i.e., the static equilibrium.

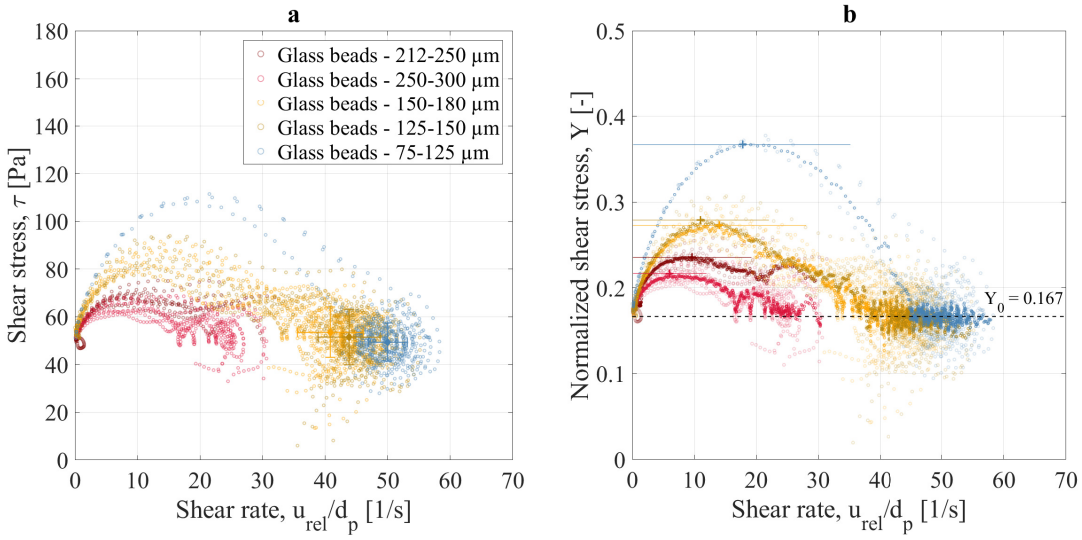

Figure 3.12: Relationship of the shear stress to the shear rate of a stagnating tracer (10_4) in five incipient fluidized beds of glass beads with varying size. a) Shear stress vs. shear rate. b) Normalized shear stress vs. shear rate.

For some of the stagnating tracers, which for a period of time exhibit an oscillation around a relatively constant falling velocity, the effective viscosity can be obtained from the center of mass, as described earlier. The stagnation curve, obtained from 10 repetitions, is evaluated by applying a moving average, identifying the maximum stress (indicated as + in Figure 3.12b) and fitting the Herschel-Bulkley model to the low shear rates. It should be noted that the higher the shear rate (the falling velocity), the higher is the maximum stress obtained from the stagnation curve.

Figure 3.13 shows the relationship between the shear stress and the shear rate of a rising tracer (20_9) in four different beds of glass beads with: a) shear stress vs. the shear rate; and b) the normalized shear stress vs. shear rate. The rising tracers exhibit a significantly different behavior than the falling tracers, performing a movement in which the gravitational and stress forces seems to be in balance at any specific time-point as the shear rate increases. The filtered data (Figure 3.13b) reveal that the shear stress is nearly constant with the shear rate, with the normalized shear stress being very close but always just below the yield gravity parameter, Y_0. This slight dominance of the gravity effects (here, buoyancy effects because the tracer is positively buoyant), enables the slow rising of the tracer.

The inherent variance of the flow behaviors of rising objects has been summarized by Chhabra [110], who observed a spiral motion as bubbles ascended through pseu-

doplastic fluids, as discussed in more detail in **Paper V**. Similar trajectories were observed for some of the rising tracers in the incipient fluidized beds. Despite the fact that various beds were tested, no significant influence of the bulk solids properties (size, sphericity, density) on the movement of the rising tracers was identified.

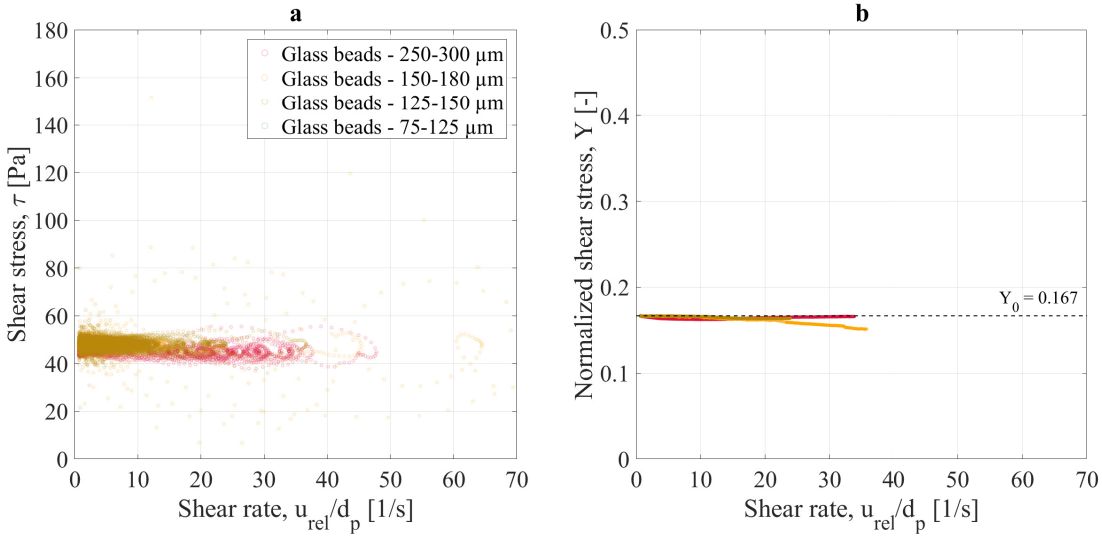

Figure 3.13: Relationship of the shear stress to the shear rate of a rising tracer (20_9) in three incipient fluidized beds of glass beads with varying size. a) Shear stress vs. shear rate. b) Normalized shear stress vs. shear rate.

In order to deduce a correlation for the shear stress so that it can be used in the model to resolve Eq. 2.10, a fitting to the experiments of the stagnating tracers in the incipient bed of bronze (ρ_{em}=5144 kg/m^3, d_s=75-125 µm) was carried out. It should be noted that, although the modeled biomass fuel particles are positively buoyant, the data from stagnating tracers was used. This is motivated by the fact that the above discussed typical rising motion was not observed for the trajectories obtained from the experiments at bubbling conditions.

Furthermore, the shear rates achieved in the model are generally low, i.e., within the range of 0-7 s^{-1}, which is the interval applied for fitting the Herschel-Bulkley model, yielding a determination coefficient of $R^2 = 0.799$. In fact, when modeling the most-buoyant particle (biochar, $d_p = 0.04$ m, $\rho_p = 400$ kg/m^3), 66% of the shear rates experienced by the particle were <0.06 s^{-1}, with 98% of the shear rates being <7 s^{-1}. This means that the motion of the particle is dominated by the yield stress, with only a small contribution from the shear stress, and within the applied shear rate range the correlation of the stagnating tracers provides a reasonable approximation for both the rising and the falling stagnating tracers.

Figure 3.14 shows the filtered normalized shear stress for the different stagnating tracers, including its the modeled curve using Eq. 3.6, reading as follows:

$$Y = \frac{\tau}{g d_p(\rho_{em} - \rho_p)} = 0.167 + 0.032 \cdot \left(\frac{u_{rel}}{d_p}\right)^{0.336} . \tag{3.10}$$

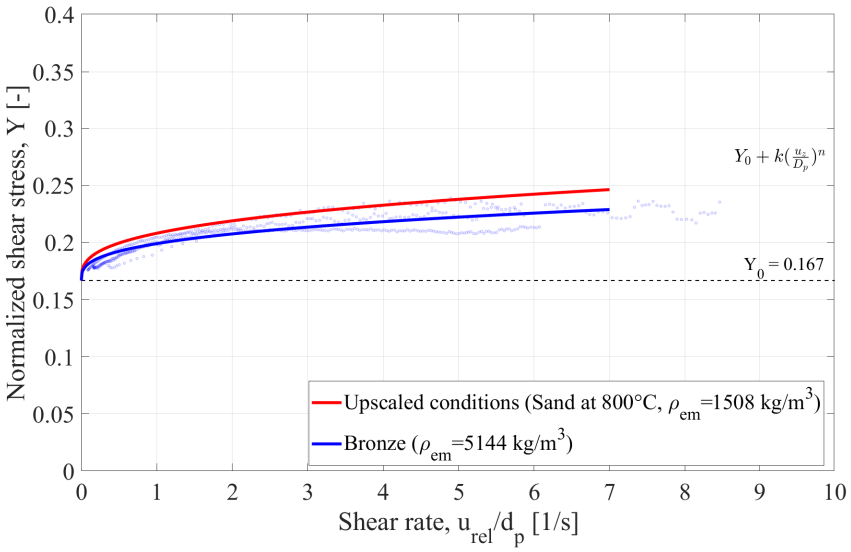

Figure 3.14: Fitting of the normalized shear stress vs. shear rate. The experiments with the stagnating tracers in the incipient bed of bronze (ρ_{em}=5144 kg/m^3, d_s=75-125 µm) are fitted. The correlation is then upscaled to hot conditions as used in the model.

Bronze was used to enable the possibility to upscale the correlation to the conditions applied in the model (sand at 800°C, ρ_{em}=1508 kg/m^3), while scaling reasonably well using the time-scaling of $2.2t$, as presented in Table 3.2. Note that only the normalized consistency index with the units of $[s^n]$ is scaled, as the other parameters are dimensionless. The fitting is also shown in Figure 3.14.

Equation 3.11 for hot upscaled conditions reads:

$$Y = \frac{\tau}{g d_p(\rho_{em} - \rho_p)} = 0.167 + 0.042 \cdot \left(\frac{u_{rel}}{d_p}\right)^{0.336} . \tag{3.11}$$

Figure 3.15 depicts the influence of the description of the drag force, either modeled with the shear stress correlation in Eq. 3.11 or with a constant (upscaled) viscosity of 1.24 Pa s, as taken from [104], on the axial mixing of a fresh biomass particle, for a low and a high fluidization velocity.

Using the shear stress correlation improves the mixing of the particle into the bed and, therefore, becomes important when modeling the mixing of heavier particles at higher fluidization velocities, as the particle exhibits a less-flotsam-like behavior and mixing inside the bed becomes more important.

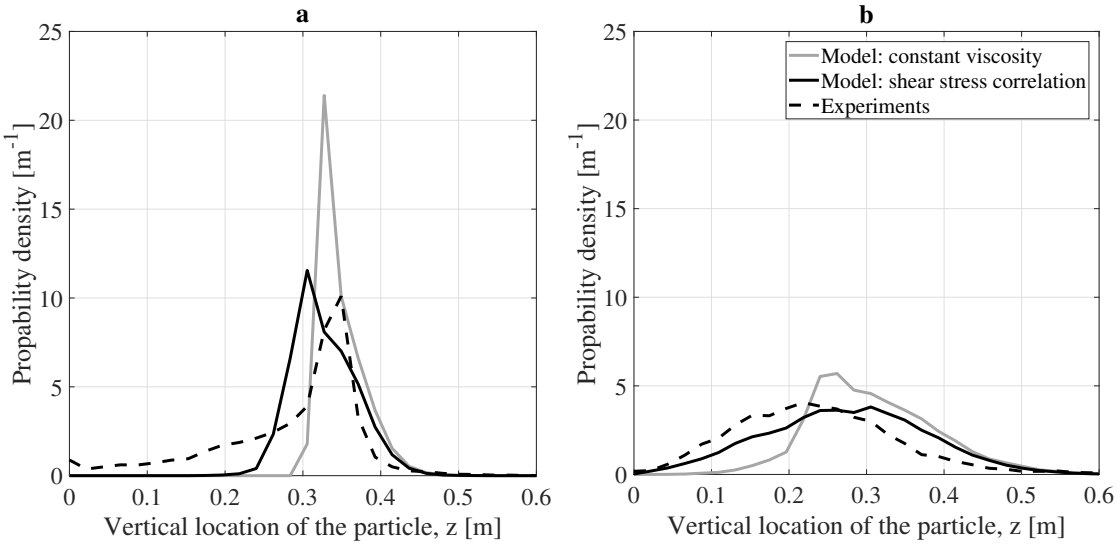

Figure 3.15: Influence of the shear stress correlation (Eq. 3.11). Modeled and experimental probability density function of the vertical location of the fresh biomass particle (d_p = 0.04 m, ρ_p = 810 kg/m^3). H_0 = 0.3 m. a) u_0 = 0.18 m/s. b) u_0 = 0.48 m/s.

4 Model validation

The validation of the model presented in Chapter 2, is divided into the validation of the model for axial fuel mixing and the validation of the model for lateral fuel mixing. The performance of the model for axial mixing is validated with measurements conducted in the fluid-dynamically downscaled bed, as presented in Chapter 3 (**Papers I** and **IV**). As for the lateral mixing, the model is validated against experimental data from three different large-scale FB units measured under both hot and cold conditions (**Paper II**).

4.1 Axial mixing

The axial mixing of large particles is known to be influenced by the operational conditions (mainly, the fluidization velocity) and by the physical properties (mainly, the size and density) of the studied particles [39, 47]. Thus, the model presented in **Paper I** is validated against experimental data including variations in those parameters sampled in the fluid-dynamically downscaled bed with bronze powder and air at room temperature, which resembles a bed of sand fluidized with air at 800°C, as presented in Table 3.2. Note that the model considers spherical particles only, so the influence of particle shape is not discussed in this work.

Figure 4.1 compares the measured and modeled probability density functions (PDF) of the vertical location of a biomass particle for two fluidization velocities and two biomass densities.

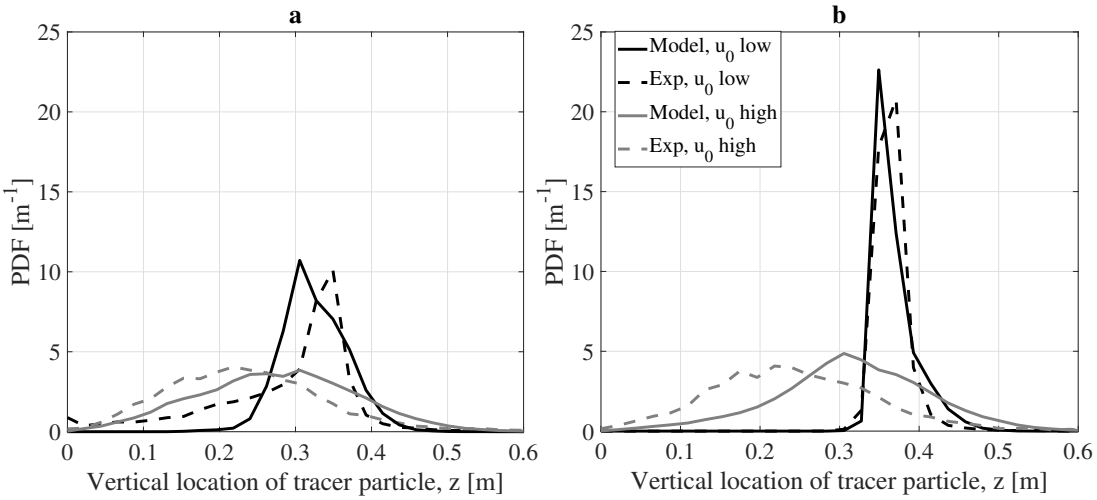

Figure 4.1: Probability density function of the modeled and measured vertical location of the fuel particle (d_p= 0.04 m) for two different excess velocities ($u_0 - u_{mf}$=[0.13;0.43] m/s). a) Fresh biomass (810 kg/m^3). b) Biochar (400 kg/m^3).

The model reproduces accurately the distributions observed in the experiments, i.e., increasing the fluidization velocity results in the particle being mixed into the bed to a greater extent, with the lighter biochar particles being more prone to float on the bed surface at low fluidization velocities. The axial segregation of the fuel can be represented as the fraction of time spent by the particle on and above the dense bed surface. Figure 4.2 plots the measured and modeled values for this time fraction against the fluidization velocity for the two biomass densities studied.

Regarding the dense bed height, it should be noted that the experimental value was determined through tests conducted with a fully flotsam tracer. These tests give a statistical distribution of values that reflects the fluctuating nature of the dense bed height due to the strong fluidization dynamics, whereas the model uses a single value (the mean of the cited experimental distribution).

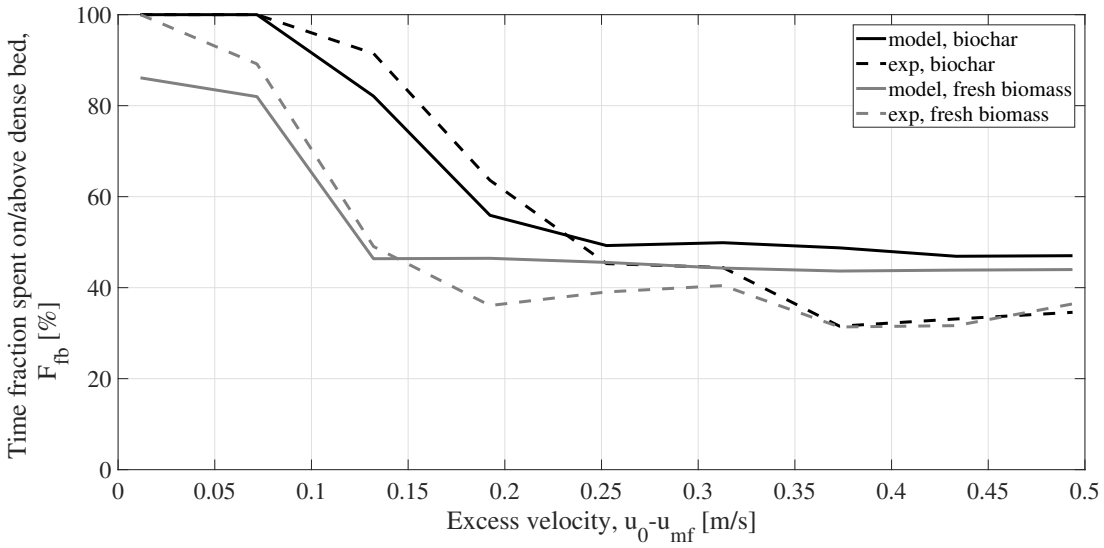

Figure 4.2: Time fractions that the fuel particle spent on and above the dense bed surface, F_{fb}, versus excess gas velocity, u_0-u_{mf}, comparing the modeling and experimental data for biochar (400 kg/m^3) and fresh biomass (810 kg/m^3).

In the experimental work, three mixing regimes have been identified for tracers with typical fuel particle densities, which are also reproduced by the modeled data: 1) a purely flotsam regime that occurs at low fluidization velocities; 2) a transition regime, for which an increase in fluidization velocity results in a rapid decrease of the time the fuel particle is present at the bed surface; and 3) a fully developed mixing regime in which the time the particle is present at the bed surface and the splash zone remains constant with fluidization velocity. The onset velocities between these regimes depend mainly on the tracer properties. Note that although the model was able to reproduce the three above-mentioned regimes and to provide a PDF for the tracer axial location that was in good agreement with the experimental results, the fully developed mixing regime of the modeled data has a systematic higher proportion of tracer observations

on the bed surface than the regimes in the corresponding experiments. The main reason for this is that the modeling uses a constant value of the dense bed height, while the dense bed height fluctuates strongly in the experiments. Thus, in the experiments, a tracer particle floating on the dense bed surface when the dense bed is below its time-averaged height will be counted as immersed, which complicates the quantitative comparison of the model and the experimental measurements.

4.2 Lateral mixing

A crucial design and operational parameter in FBs for solid fuel conversion is how fast the fuel particles spread laterally over the cross-section of reactor, which is large in relation to the bed height in commercial-scale units. At the macroscopic level, the lateral mixing of fuel in the bottom region of the unit can be approached as a stochastic process that is characterized by a lateral dispersion coefficient, $D_{x,y}$. The values for this coefficient listed in the literature vary with several orders of magnitude, with a strong dependence on the cross-sectional area of the reactor being demonstrated by Sette et al. [96].

Both in the model and in the experiments, the lateral dispersion coefficient is calculated from the trajectory data using the Einstein equation [114] for Brownian motion:

$$D_{x,y} = \frac{\Delta(x,y)^2}{2\Delta t} \tag{4.1}$$

This work considers quadratic recirculation cells, i.e., cells of equal width and depth, for the general case of designs with equal nozzle spacing in the x- and y-directions, resulting in isotropic mixing of the large particles in the lateral directions, i.e., $D_x = D_y = D_{lat}$.

4.2.1 Statistical robustness

The statistical representability of the modeled data is tested by simulating 15-min-long trajectories of a fuel particle using the input data from Qian et al. [115] (Table 1). The final location of the particle in each simulation provides a value for the lateral dispersion coefficient according to Eq. 4.1, which when summed yield a distribution of the dispersion coefficient values. Since the motion of fuel particles in a BFB is a stochastic process, the lateral dispersion coefficient follows a statistical distribution. Figure 4.3 displays some of the statistical parameters for this distribution, namely the mean, the median, and the upper and lower quartiles, and shows how these parameters develop with the number of simulated trajectories of a single fuel particle. Finally, a boxplot of the lateral dispersion coefficient for a simulation of the motion of 1000 trajectories is included, showing the entire statistical distribution in a compact way. The box, which is bounded by the lower and upper quartiles, represents the

values higher than 25% and 75% of the data in the distribution, respectively. The line in the middle of the box represents the median, which is the value greater than 50% of the data in the distribution. The boxplots include also confidence intervals for the data, represented by dashed lines (called *whiskers*), which are calculated as the last data-points of the distribution found at a maximum distance of 1.5-times the interquartile distance from the upper or lower quartile. Any data outside these confidence intervals are designated as *outliers*, i.e., data-points with a low probability of occurrence, ordinarily represented as singular points in the plot. For the sake of simplicity, they are not presented in the figure. The distribution of lateral dispersion coefficients represented by the boxplot shown in Figure 4.3 is non-normal, as different values are obtained for the mean and the median and the boxplot is not symmetric with respect to the median. Therefore, instead of the mean and the standard deviation, which are the representative values for a normal distribution, the median and quartiles reported in the form of boxplots are used as representative values for the non-normal distribution of the lateral dispersion coefficients.

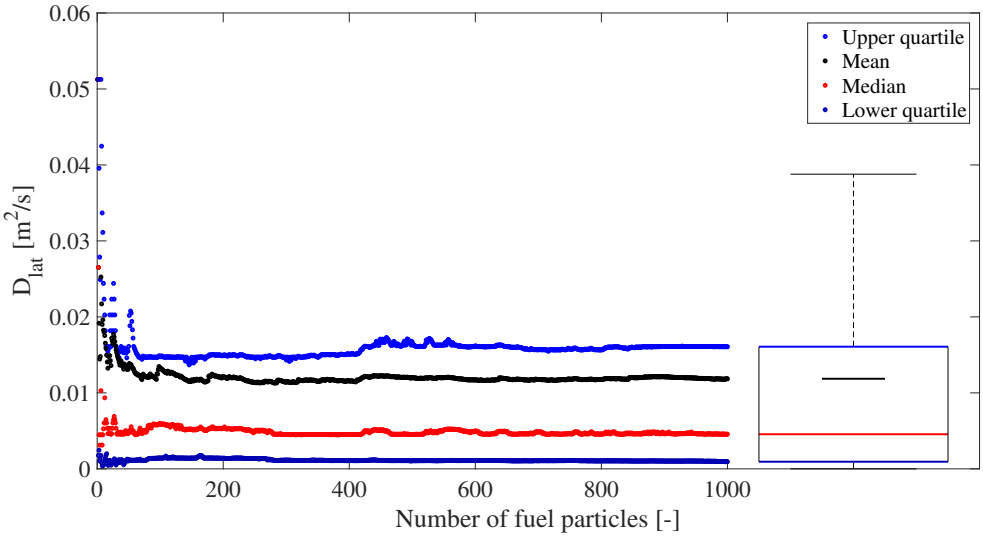

Figure 4.3: Effect of the number of fuel particles included in the simulation on the lateral dispersion coefficient. Modeling case: that of Qian et al. [115] with a gas velocity of 1.03 m/s.

As shown in Figure 4.3, the distribution of the lateral dispersion coefficient becomes relatively stable when one considers approximately 500 simulations, and is highly reliable when one examines more than 700 simulations.

Finally, it should be noted that while statistical robustness is attainable in the evaluation of the modeled lateral dispersion coefficient, the experimental data face the challenge of dealing with finite geometries, and this often limits the ability to extract statistically robust experimental values. Therefore, it is not certain how robust the experimental values reported in literature are, since they are derived from finite geometries and for a limited number of fuel particles.

4.2.2 Input data and validation

In order to validate the 3D model in terms of its performance in simulating lateral dispersion under conditions relevant for industrial units, data from three different experimental campaigns [34, 99, 115] conducted in large-scale FBs under both hot and cold conditions are used. Table 4.1 summarizes the input parameters from the experimental setups simulated with the model.

Qian et al. [115] conducted experiments under cold bubbling conditions in a rectangular boiler area of 4.16 m^2 and obtained the lateral dispersion coefficients of continuously fed spherical bituminous coal particles (1340 kg/m^3, 14 mm) at different fluidization velocities (0.68-1.03 m/s) and with three different bed heights (0.25, 0.30, and 0.35 m). They used a rather coarse sand as the bed material (2600 kg/m^3, 1420 µm), with a minimum fluidization velocity of 0.63 m/s. To obtain the lateral dispersion coefficients, they measured the fuel concentration by collecting the fuel particles from 15 compartments of a grid over the bed in several rounds. The procedure was continued until all the tracer particles were dispersed equally over the bed. As the distribution of the nozzles inside the bed was not provided in that work [115], it is assumed that they used the same bubble catchment area of 0.0201 m^2 as given in [99], which applies to a typical industrial-scale boiler of similar size.

Niklasson et al. [99] measured the lateral fuel dispersion at a temperature of 900°C in a square boiler of area 2.89 m^2, using a 9-point grid of moisture measurements over the cross-section of the bed to obtain the concentration of continuously fed wet biomass particles as they spread. They used sand (2600 kg/m^3, 700 µm) with a minimum fluidization velocity of 0.17 m/s, and their operational conditions included a gas velocity of 2.30 m/s at a bed height of 0.5 m. The fuel density was not given but was estimated to be around 810 kg/m^3. The fuel particle size is given as the log-normal distribution of the surface area divided by the volume with a mean of 710 m^{-1} and a standard deviation of 290 m^{-1}, resulting in an equivalent diameter of 0.008 m. However, given that the shape factor of wood chips is much less than 1, the projected area required to solve the equation of motion is expected to be much higher. Thus, the model applies an equivalent diameter of a single particle with a projected area of 32.5×32.5 m^2 as reported by [34], resulting in an equivalent diameter of 0.37 m. The effect of the particle diameter on the lateral dispersion was investigated and is discussed in Chapter 5.

Olsson et al. [34] carried out measurements of the lateral dispersion coefficient in a cold BFB with a rectangular cross-sectional area of 1.44 m^2 and a bed height of 0.4 m. The bubble catchment area was 0.0201 m^2. The bed material consisted of sand particles (2600 kg/m^3, 150 µm) with a minimum fluidization velocity of 0.02 m/s. They applied ambient air as the fluidizing gas with fluidization velocities of 0.10 m/s and 0.15 m/s. In seven repetitions of batch experiments with 15-20 bark pellets particles in each (523.5 kg/m^3, 0.013 m), the lateral dispersion coefficient was

Table 4.1: Input parameters for validation of the 3D model in simulating lateral dispersion.

Variable	Qian et al. (1987) [115]	Niklasson et al. (2002) [99]	Olsson et al. (2012) [34]
Bed cross section, m^2	$2.6 \times 1.6 = 4.16$	$1.7 \times 1.7 = 2.89$	$1.7 \times 0.85 = 1.44$
Bubble catchment area, m^2	0.0201	0.0201	0.0241
Bed material particle density, kg/m^3	2600	2600	2600
Bed material particle size, µm	1420	700	150
Temperature	ambient	900°C	ambient
Minimum fluidization velocity, m/s	0.63	0.17	0.02
Bed height, m	0.25; 0.30;0.35	0.5	0.4
Gas velocities, m/s	0.68; 0.75; 0.86; 1.03	2.30	0.10; 0.15
Fuel	Continuous feed of spherical coal	Continuous feed of wood chips with moisture of 45%	Batches of 7×15 particles, bark pellets
Fuel density, kg/m^3	1340	810	1180
Fuel particle size, equivalent diameter, mm	14.0	37.0	12.8

measured by digital image tracking of the individual particles, which were equipped with small phosphorescent plastic capsules. They limited the experimental time to 6 min and 30 s and calculated the final lateral dispersion coefficient by averaging the dispersion coefficients measured over a period of 5 min. If a particle reached the opposite wall earlier than 5 min, the average was taken from the reduced time period. Note that they used cylindrical particles (21×8 mm), for which an equivalent diameter of 0.013 m is taken as an approximation.

In this work, 1000 simulations are considered for calculating the lateral dispersion from the modeling of the experimental input given in Table 4.1. This is in line with the experimental procedure, which was based on continuous fuel feeding for several minutes (corresponding to thousands of fedfuel particles). On the other hand, the results presented by Olsson et al. [34] for a certain set of conditions were based on seven repetitions of tests with 15-20 fuel particles each. An average dispersion coefficient for the whole batch was calculated as the first fuel particle of the batch to reach the wall. This limited the number of particles and observation time results for rather low dispersion coefficients with a rather large statistical uncertainty, as discussed already by Olsson et al. [34]. To ensure alignment with the experimental procedure, the model was set to simulate 1000 repetitions of batches consisting of 15 fuel particles each.

Figure 4.4 shows the distribution of the 1000 simulated tests for the datasets of the three different experiments from: a) Olsson et al. [34], b) Qian et al. [115], and c) Niklasson et al. [99], using the respective input parameters presented in Table 4.1. The experimental results from each campaign are indicated with open circles ($\circ$) in the plots. It is clear that most of the experimental values lie within the quartiles of the distribution, i.e., within the 25% and 75% percentiles, represented in the boxplots derived from the 1000 modeled trajectories for each case. In fact, only some of the experimental results from Olsson et al. [34] present values that lie outside the quartiles of the dispersion coefficient distribution.

However, despite the relatively broad dispersion of these experimental values, they lie within the confidence interval of the distribution, as represented by the whiskers of the boxplot. It must be emphasized here that the model is capable of representing a wide range of experimental values for the dispersion coefficients (spanning three orders of magnitude), with fluidization numbers in the range of 1.1–13.5 m^2/s. The model is also able to follow the trend of increased lateral dispersion that occurs with an increase in fluidization velocity, as shown in Figure 4.4b.

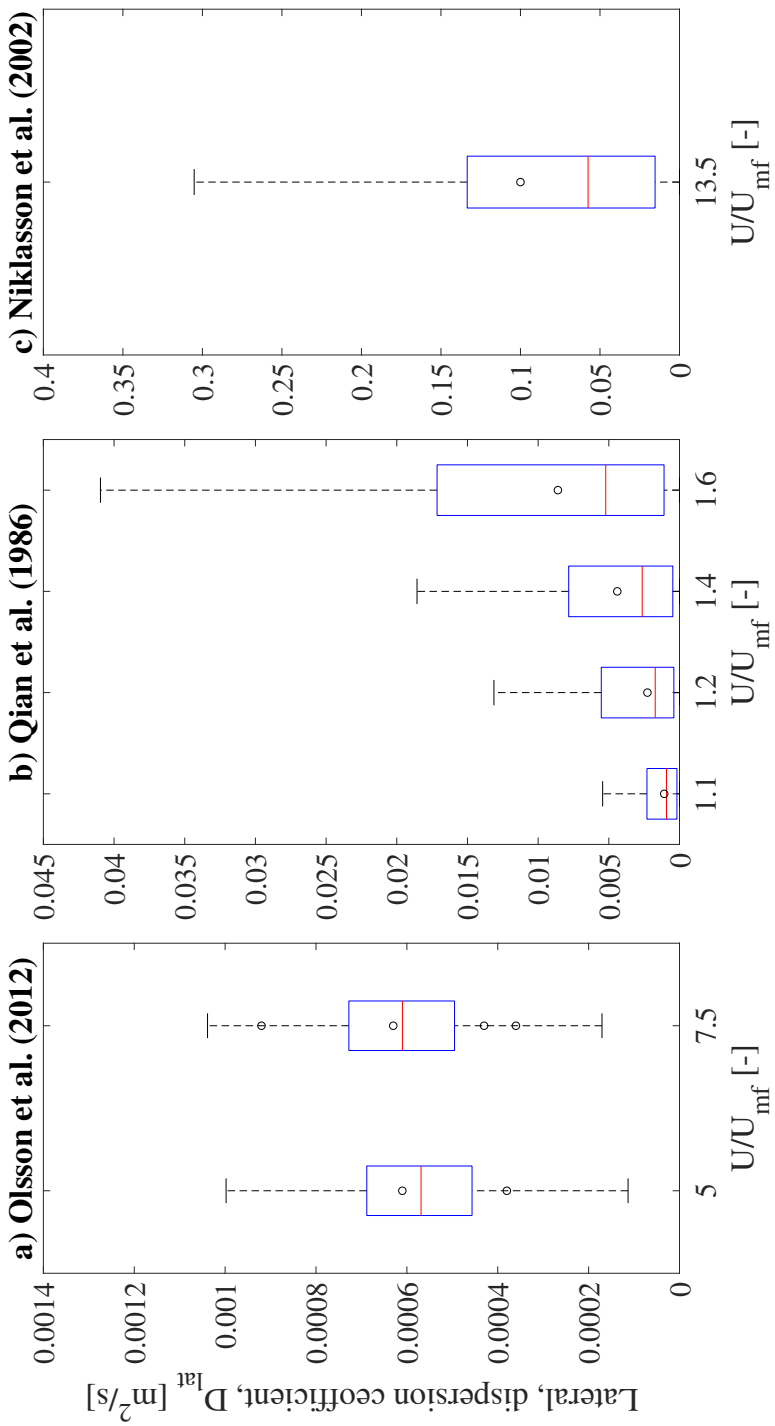

Figure 4.4: Model validation comparing the lateral dispersion coefficients from three different experiments described in the literature: a) Olsson et al. [34]; b) Qian et al. [115]; and c) Niklasson et al. [99]. Experimental results are indicated with open cicles (○) in the plots. Note the different scales on the y-axis.

5 Selected results: Factors impacting mixing

This chapter summarizes selected results of the work, which contribute to improving the understanding of the mixing of large particles in FBs. The results are presented in terms of the impacts that the most significant factors (Figure 1.3) have on the mixing. For more detailed results the reader is referred to the appended papers.

5.1 Bed material properties

Depending on the application and the fuel used, the bed material can vary with respect to the size, shape and density of the solids, which influence the flow properties, thereby affecting the mixing of the fuel in the bed. **Paper VI** investigates how these bed properties influence the rheological behaviors through the use of falling sphere experiments in incipient FBs with various combinations of bed materials and tracers (Table 3.4). Figure 5.1a compares the effective viscosities of two different materials of similar density (2570 kg/m^3) but with different sphericities (glass beads, 1; and sand, 0.75) in two different sizes (125-250 µm, 75-125 µm).

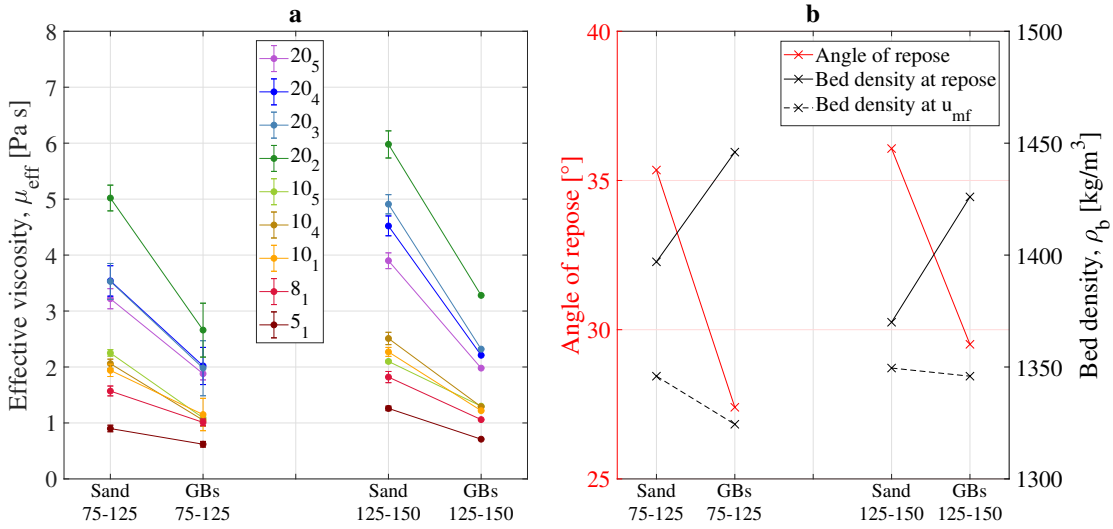

Figure 5.1: a) Effective viscosity experienced by different tracers falling through incipient fluidized beds, varying bulk solids sphericity and size. b) Angle of repose and bed density (at rest and at u_{mf}).

As shown in Figures 3.11 and 3.12, decreasing the bulk solids size results in higher shear rates fluctuating around the dynamic equilibrium. This means that the deceleration caused by the drag force of the emulsion on the particle is lower, yielding a

lower viscosity for beds with smaller bulk solids, as seen in Figure 5.1. Decreasing the sphericity lowers the shear rates experienced by the falling tracer and results in higher effective viscosities.

Figure 5.1b displays the angle of repose and the density of the bed at repose and at minimum fluidization. Both the size and sphericity of the bulk solids affect the bed density at minimum fluidization, which follows the trend of the viscosity, i.e., increasing the bed density results in a higher effective viscosity. The resistance of the emulsion to the motion of the tracer is related to the ability of the solids to make space for the tracer. This resistance is higher for a higher bed density at u_{mf}. Furthermore, the angle of repose and the density at repose of the bed give information about the flow properties of the bed at rest with a higher angle and a lower density, implying a higher degree of interlocking of the solids, resulting in higher internal forces. When the bed is fluidized, this translates into a higher bed density at u_{mf}, thereby exerting a higher resistance to the intrusion of the tracer, i.e., a higher effective viscosity. This trend is also supported by Eq. 3.8, indicating that the shear stress, from which the viscosity is calculated, is increasing as the emulsion density increases.

The influence of viscosity on the mixing of the fuel has been studied with the axial model in **Paper I**. The results show that mixing of the fuel into the bed is enhanced with increasing viscosity, as the drag force of the downwards flowing solids increases.

5.2 Operational conditions

Operational conditions that are typically varied in FB reactors are the fluidization velocity, the bed height, the pressure drop over the bed (i.e., the bed height) and over the gas distributor, and the temperature in the reactor. The impacts of the various conditions were investigated through modeling in **Papers I** and **II** and experimentally in **Papers III** and **IV**.

The temperature in the reactor is controlled by a combination of the heat provided by the incoming fluidization gas and the incoming bed material (e.g., indirect gasification) and the heat of reaction for the fuel conversion. In this work, temperature is discussed in connection with fluid-dynamic scaling and is shown to have a major role when studying mixing in scaled experiments resembling hot conditions and comparing the results to plain cold tests without scaling. Given that increased temperature enhances the size and velocity of the bubbles in the bed, the mixing of solids and fuel is also enhanced, as discussed in **Paper IV** and in Section 3.2.

The pressure drop over the gas distributor is not only a function of the fluidization velocity, but also a property that is dependent upon the design configuration of the gas distributor. The mixing that results from various combinations of the pressure drop over the distributor and over the bed height was studied in **Paper III** using four different distributor plate designs and various dense bed heights. The effects of the distributor pressure drop on the 3D probability density function of a larger

particle for two different plates are depicted in Figure 5.2. For the low gas distributor pressure drop (a), the particle shows a jetsam behavior with stagnant zones along the walls in the bottom of the bed. Axial mixing is promoted by a high gas distributor pressure drop forming prominent toroidal flow structures around each rising bubbles path, of which 2×2 can be identified in Figure 5.2b. It should be noted that due to the cost of fan power, the pressure drop is usually low in large industrial applications, while gas distributors in laboratory units are often designed with high pressure drops, to ensure adequate fluidization over a wide range of fluidization velocities.

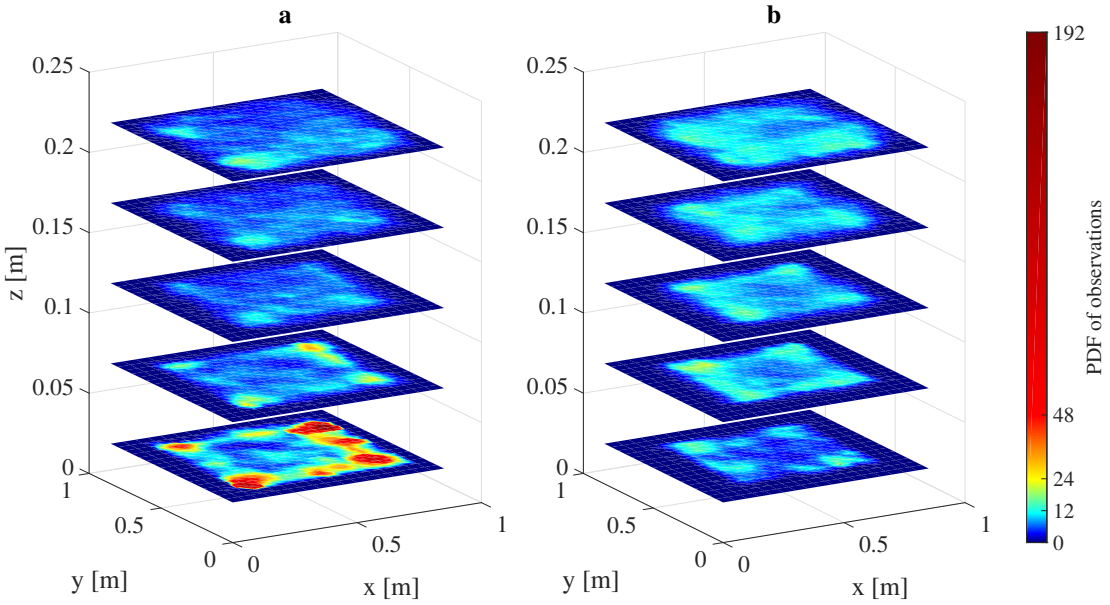

Figure 5.2: Experimental results from MPT measurements in the fluid-dynamically downscaled bed. Effect of the air distributor pressure drop on axial mixing. PDF of the tracer locations of a cylindrical particle resembling coal (L_p=0.015 m, d_p=0.03 mm, ρ_p=1890 kg/m^3) in the fluid-dynamically downscaled bed at u_0-u_{mf}=0.15 m/s and H_0=0.25 m. a) Low gas distributor pressure drop. b) High gas distributor pressure drop.

The effect of fluidization velocity on the mixing of large particles is discussed in **Papers I**, **III** and **IV** (axial direction) and **Papers II** and **III** (lateral direction). With increased fluidization velocity, the bubbles grow larger and rise faster through the bed, such that they carry more bed material in their wake and induce more-vigorous convective axial mixing of both the bulk solids and large particles. This may decrease the tendency of the fuel, which is flotsam in nature due to its lower density and larger size, to segregate on the bed surface, as shown by measurements and described by modeling (Figure 4.2). The observed saturation in this trend occurs because the more-vigorous bubbling reduces the rising velocity of the fuel (Figure 3.6). As bubbles grow larger, the sizes of the recirculation cells increase, promoting lateral fuel mixing, as shown in the modeling results in Figure 5.3. Furthermore, an increased fluidization velocity leads to a widening of the statistical distribution of the dispersion coefficients.

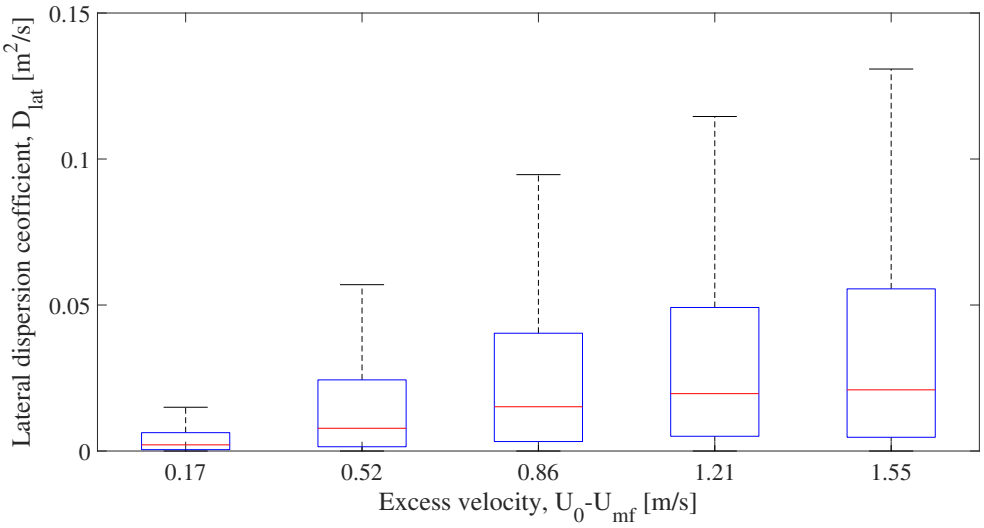

Figure 5.3: Modeling results. Effect of the fluidization velocity on the lateral distribution coefficient of wood chip particles in an industrial-scale FB operated under hot conditions, H_b=0.5 m.

The bed height is mainly coupled to the amount of bed material in the reactor and may increase or decrease during operation due to the entrainment and feeding and discharge of bulk solids or fuel ash. The effect of the bed height on the lateral mixing is discussed in **Paper II** and the effect on axial mixing is dealt with in **Papers III** and **IV**. Increasing the bed height increases the axial mixing of both bulk solids and large particles as the bubbles grow bigger and the axial convective flows of the bulk material (both upwards in the bubble wake zone and downwards in the emulsion zone; see Figure 2.1) are improved and, as a consequence, the mixing of the large particles is enhanced. However, when the effect of the bed height on the lateral mixing of fuel (through the dispersion coefficient) was investigating with the model, little influence was found (**Paper II**).

This can be explained by the relative time spent and distance travelled by the tracer inside the bed and in the splash zone, respectively, as depicted in Figure 5.4. While a higher fluidization velocity results in fuel particles spending more time in the splash zone, due to the eruptions of more-vigorous bubbles causing longer ballistic trajectories, increasing the bed height leads instead to a higher time fraction spent inside the dense bed. This reduction in time spent in the splash zone, which is more effective in terms of lateral mixing, in combination with the fact that the lateral distance travelled stays constant due to fewer but more-vigorous ejections, results in the lateral dispersion being hardly affected.

The bed height has, by means of the modified extent of bubble coalescence, a direct impact on the number of recirculation cells. This can be seen from the fluid-dynamically downscaled experimental data represented in Figure 5.5, showing the flow structures of a cylindrical tracer that resembles coal (H=0.015 m, d_p=0.03 mm,

ρ_p=1890 kg/m^3) in a bed fluidized at u_0-u_{mf}=0.22 m/s. The tracer is transported upwards in the centre of the recirculation cells (red) and sinks along the sides of the cell (blue). Comparing Figure 5.5a (H_b=0.15 m) with Figure 5.5b (H_b=0.25 m), it is clear that increasing the bed height leads to a decrease in the number of mixing cells, which in turn affects the lateral mixing.

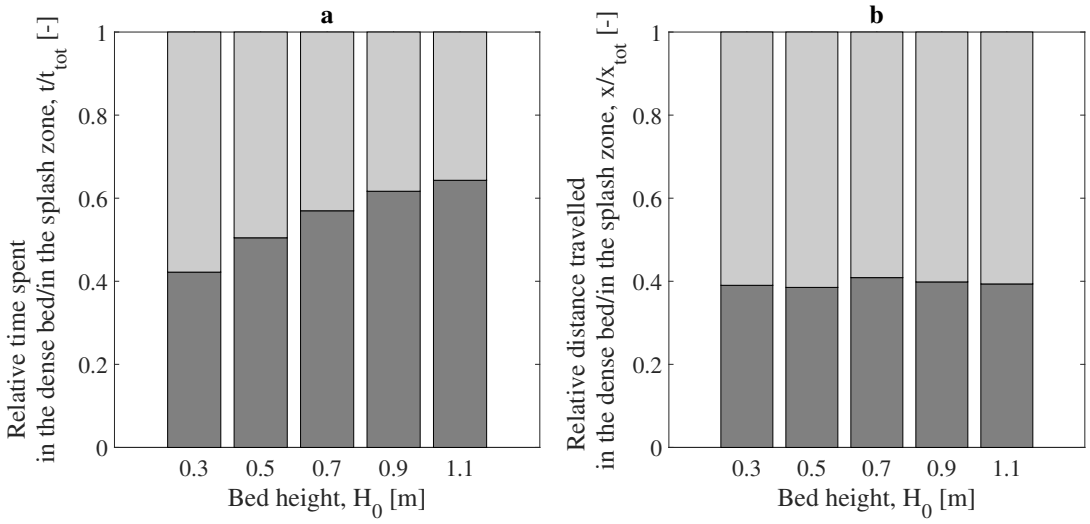

Figure 5.4: Modeling results. Effect of bed height on the lateral mixing of wood chips particles in an industrial-scale FB operated under hot conditions, u_0-u_{mf}=0.86 m/s. a) Fraction of time spent by the tracer in the dense bed and splash zone. b) Fractions of effective displacement of the tracer in the dense bed and splash zone.

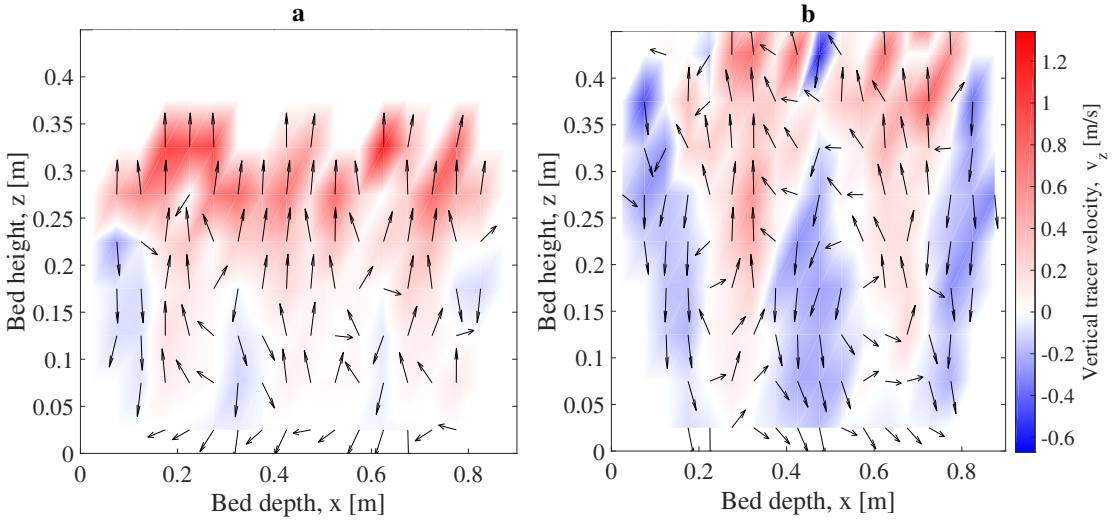

Figure 5.5: Experimental results. Effect of the bed height on the number of recirculation cells visualized with the flow structures of a cylindrical tracer that resembles coal (H=0.015 m, d_p=0.03 m, ρ_p=1890 kg/m^3) in the fluid-dynamically downscaled bed at u_0-u_{mf}=0.22 m/s. a) H_b=0.15 m. b) H_b=0.25 m.

5.3 Fuel properties

Different fuels can be used in FBs (Table 1.1), and the fuel particles, which can be found inside the reactor, vary significantly in terms of physical properties (size, density and shape). This work focus on woody biomass in different forms (wood chips and pellets) and conversion stages (fresh, dried, pyrolysed). The properties investigated are fuel density and size, while the shapes used are spheres (**Papers I**, **II** and **IV**) and cylinders (**Paper III**).

Lighter and larger particles are more prone to segregate axially on the bed surface, especially at low fluidization velocities (Figure 4.1). This is because as the volume increases with d_p^3 the buoyancy force becomes dominant for larger particles, while the drag force (scaling with the projected area, i.e., d_p^2) is more prominent for smaller particles. The onset velocity from which the particle mixes into the dense bed, is higher the lighter the particle (Figure 4.2).

In a FB reactor, the fuel particles undergo conversion, i.e., their size and/or density are continuously changing. The effect of this on axial mixing was simulated for a fresh biomass particle with 8 wt% moisture and a char yield of 47 wt%. Dividing the bed into three areas (dense bed, bed surface, and splash zone), Figure 5.6 shows the modeled probability of the particle being present in each area, while drying and devolatilization (shrinking core) and char conversion (shrinking sphere) take place (combustion in air at 800°C).

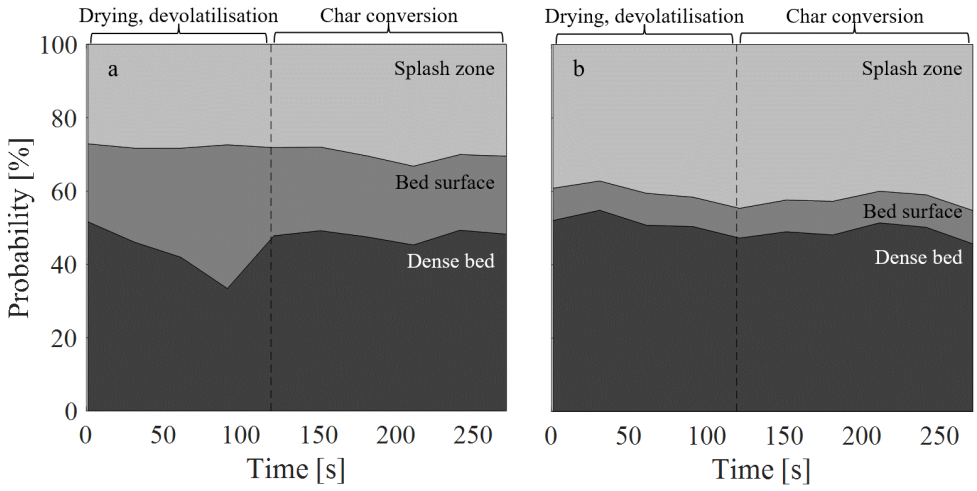

Figure 5.6: Modeling results. Effect of fuel properties (size, density) on axial mixing during conversion in the bottom region of a FB expressed as the probability of a biomass particle (d_p= 0.04 m, ρ_p= 813 kg/m^3) being present in the different areas of the bed over time. a) Low excess velocity u_0-u_{mf}=0.13 m/s. b) High excess velocity u_0-u_{mf}=0.37 m/s.

It can be seen that at a low fluidization velocity (a), the decrease in density during drying and devolatilization increases the flotsam behavior of the fuel particle, while the decrease in size during char conversion has little influence in this respect. It

should be noted that the release of volatiles adds a lifting force to the particle, which is shown in **Paper III** to contribute significantly to the segregation of the particle, especially at low fluidization velocities. At a high fluidization velocity (b), axial mixing of the fuel remains essentially independent of the changes in fuel properties. These and further findings related to the effects of fuel size and density on the lateral dispersion of the fuel are presented in **Paper II**.

6 Conclusion

6.1 Summary and main findings

With the aim to facilitate the upscaling of commercial units and to favor the design of new applications, this thesis advances the understanding of the mixing of solids (especially those representative of fuel particles) in the dense region of FBs. To achieve this, the thesis exploits semiempirical modeling, different experimental approaches, and their various interconnections.

The semiempirical 3D model was based on a bubble flow description with established correlations from the literature, on which a mechanistic description of the motion of spherical particles with various fuel properties was implemented. For closure of the model, empirical input was obtained through magnetic particle tracking (MPT) in a fluid-dynamically downscaled bubbling bed and in different incipient fluidized beds. The scaled experiments were designed to provide data that were representative of hot large-scale conditions, which were shown by both the model and the experimental work to be crucial for describing mixing in industrial units, rather than in laboratory-scale beds.

The use of the model identified three parameters to enable a satisfactory description of the fuel mixing: 1) the wake volume of rising bubbles - fitting in the model showed this to yield values up to 2-fold higher than the values deduced from cold units reported in the literature; 2) the rising velocity of fuel particles - the experimental work found this to be much higher than the values predicted in the literature; and 3) the effective drag of the surrounding emulsion zone on the immersed particle - this has been scarcely studied in the literature, so it was further evaluated in this thesis with experiments.

After developing modeling and experimental tools to facilitate a better understanding of mixing, this thesis focuses on disentangling the rheological behavior of incipient fluidized beds by means of an extensive MPT measurement campaign that combined different bed materials and spherical tracers (both jetsam and flotsam). This was designed to fill the knowledge gap related to the effective drag of the FB emulsion on an immersed particle.

The highly resolved tracer trajectories reveal a non-Newtonian flow behavior of the bed in terms of the exerted shear stress acting on the tracer. Both falling and rising tracers show a distinct yield stress, which typically represents a larger contribution to the shear stress than the drag caused by the shear rate. This effect was most pronounced for the buoyant tracers. Investigating different sizes, densities, and particle

shapes of the bulk solids reveals a reduction in effective viscosity with decreasing bulk solids size, with decreasing bulk density at minimum fluidization and for round bulk solids (as compared to sharp-edged bulk solids).

The stress patterns observed in the rheometric experiments are successfully implemented in the semiempirical model, resulting in axial distributions of the studied tracers that are closer to the experimental data used for validation.

The model developed is shown to describe appropriately the strongly varying lateral mixing (10^{-4}-10^{-1} m^2/s) of different fuel types measured in three different large-scale FB units under both hot and cold conditions.

The combination of model studies and experimental work shows that while axial mixing is fostered by increasing the fluidization velocity, bed height, distributor pressure drop or fuel particle density and decreasing the fuel particle size, only a higher fluidization velocity shows a clear influence on the lateral dispersion. This pattern can be attributed to the influence of the fluidization velocity on the widths of the recirculation cells, which are found to play a major role in the lateral mixing of fuel particles.

6.2 Recommended future work

In this work, MPT measurements ably visualized recirculation cells in beds with a cross-section yielding 2×2 cells. The performance of measurements in larger scale-models would enable a dedicated study of how the number of recirculation cells is influenced (e.g., for different gas distributor configurations), as this is here concluded to be a key parameter for the proper description of lateral fuel mixing.

This work studied inert tracer particles experimentally and the effects of changing the volume and density of converting fuel particles with modeling. The magnetic tracer used in the MPT tests could be embedded in sublimating material to evaluate the force related to the release of gases, so as to gain an understanding of how fuel mixing is affected during drying and devolatilization. It should be kept in mind that the magnetic tracers used in this work are limited to an operational temperature of 80°C, and that high-temperature Neodymium magnets are available that function at temperatures up to 230°C.

MPT in fluid-dynamical downscaled units could be complemented with simultaneous characterization of the flow of bulk solids and/or bubbles, using radar techniques or X-ray tomography. With this, the uncertainty linked to the use of empirical correlations to estimate the bubble and bulk solids flows could be substituted by experimental data and, possibly, a more accurate description of the mixing would be attained.

With the MPT technique, both the tracer position and the orientation of the dipole can be obtained, enabling an extension of the rheology studies of the gas-solids emulsion with non-spherical tracers. Such tests would provide insights into the

drag regime (viscous/inertial) and useful information about whether/how fuel shaping can be used to optimize its mixing. It should be noted that the cylindrical tracer in the freely bubbling bed used in this work showed a tendency to orient towards the magnetic North Pole of the Earth. This force can be eliminated by applying an opposing magnetic field.

It would be of interest to test the drag expression obtained in this work with a CFD model that uses a discrete phase model (DPM) for fuel particle tracking.

Bibliography

[1] IPCC. Global Warming of 1.5°C. An IPCC Special Report on the impacts of global warming of 1.5°C above pre-industrial levels and related global greenhouse gas emission pathways, in the context of strengthening the global response to the threat of climate change,. Technical report, 2018.

[2] IEA. Global Energy & CO2 Status Report 2019. Technical report, IEA, Paris, 2019.

[3] Fritz Winkler. Verfahren zum Herstellen von Wassergas. Patent DE437970C, 1922.

[4] John R Grace. Introduction, History, and Applications, apr 2020.

[5] Kinshuk Dasgupta, Jyeshtharaj B. Joshi, and Srikumar Banerjee. Fluidized bed synthesis of carbon nanotubes - A review, jul 2011.

[6] Arjen P Didden, Joost Middelkoop, Wim F A Besling, Diana E Nanu, and Roel van de Krol. Fluidized-bed atomic layer deposition reactor for the synthesis of core-shell nanoparticles. *Review of Scientific Instruments*, 85(1):13905, jan 2014.

[7] Guruprasad Alva, Yaxue Lin, and Guiyin Fang. An overview of thermal energy storage systems. *Energy*, 144:341–378, 2018.

[8] J Sunku Prasad, P Muthukumar, Fenil Desai, Dipankar N Basu, and Muhammad M Rahman. A critical review of high-temperature reversible thermochemical energy storage systems. *Applied Energy*, 254:113733, 2019.

[9] Joris Koornneef, Martin Junginger, and André Faaij. Development of fluidized bed combustion—An overview of trends, performance and cost. *Progress in Energy and Combustion Science*, 33(1):19–55, 2007.

[10] Bo Leckner. Fluidized bed combustion: Mixing and pollutant limitation. *Progress in Energy and Combustion Science*, 24(1):31–61, 1998.

[11] I Gulyurtlu, F Pinto, P Abelha, H Lopes, and A T Crujeira. 9 - Pollutant emissions and their control in fluidised bed combustion and gasification. In Fabrizio B T Fluidized Bed Technologies for Near-Zero Emission Combustion Scala and Gasification, editors, *Woodhead Publishing Series in Energy*, pages 435–480. Woodhead Publishing, 2013.

[12] Thomas Fouilland, John R Grace, and Naoko Ellis. Recent advances in fluidized bed technology in biomass processes. *Biofuels*, 1(3):409–433, may 2010.

[13] Piero Salatino and Roberto Solimene. Mixing and segregation in fluidized bed thermochemical conversion of biomass. *Powder Technology*, 316:29–40, 2017.

[14] Y H Li, Z Chen, P Watkinson, X Bi, J Grace, C J Lim, and N Ellis. A novel dual-bed for steam gasification of biomass. *Biomass Conversion and Biorefinery*, 8(2):357–367, 2018.

[15] Henrik Thunman, Teresa Berdugo Vilches, Martin Seemann, Jelena Maric, Isabel Cañete Vela, Sébastien Pissot, and Huong N T Nguyen. Circular use of plastics-transformation of existing petrochemical clusters into thermochemical recycling plants with 100% plastics recovery. *Sustainable Materials and Technologies*, 22:e00124, 2019.

[16] Henrik Thunman, Martin Seemann, Teresa Berdugo Vilches, Jelena Maric, David Pallares, Henrik Ström, Göran Berndes, Pavleta Knutsson, Anton Larsson, Claes Breitholtz, and Olga Santos. Advanced biofuel production via gasification – lessons learned from 200 man-years of research activity with Chalmers' research gasifier and the GoBiGas demonstration plant. *Energy Science & Engineering*, 6(1):6–34, feb 2018.

[17] Zhong Huang, Lei Deng, and Defu Che. Development and technical progress in large-scale circulating fluidized bed boiler in China. *Frontiers in Energy*, 14(4):699–714, 2020.

[18] S Nickull and A Kokko. The Alholmens Kraft new power plant: the world's largest biofuel fired CFB in operation. In *10. annual Power-Gen Europe*, Milan, 2002.

[19] Markus Bolhar-Nordenkampf and Matti Tiilikka. Advanced Gasification Technologies for Large Scale Energy Production. In *Power-Gen Europe 2014*, Berlin, 2014.

[20] Tobias Mattisson, Martin Keller, Carl Linderholm, Patrick Moldenhauer, Magnus Rydén, Henrik Leion, and Anders Lyngfelt. Chemical-looping technologies using circulating fluidized bed systems: Status of development, apr 2018.

[21] Juan Adánez and Alberto Abad. Chemical-looping combustion: Status and research needs. *Proceedings of the Combustion Institute*, 37(4):4303–4317, 2019.

[22] J Carlos Abanades, Edward J Anthony, Dennis Y Lu, Carlos Salvador, and Diego Alvarez. Capture of CO2 from combustion gases in a fluidized bed of CaO. *AIChE Journal*, 50(7):1614–1622, jul 2004.

[23] Borja Arias, Mónica Alonso, and Carlos Abanades. CO2 Capture by Calcium Looping at Relevant Conditions for Cement Plants: Experimental Testing in a 30 kWth Pilot Plant. *Industrial & Engineering Chemistry Research*, 56(10):2634–2640, mar 2017.

[24] IEA. Renewables information: Database Documentation (2020 Edition). Technical report, IEA, Paris, 2020.

[25] Ronald W Breault. A review of gas–solid dispersion and mass transfer coefficient correlations in circulating fluidized beds. *Powder Technology*, 163(1):9–17, 2006.

[26] A Svensson, F Johnsson, and B Leckner. Bottom bed regimes in a circulating fluidized bed boiler. *International Journal of Multiphase Flow*, 22(6):1187–1204, 1996.

[27] Anton Larsson. *Fuel Conversion in a Dual Fluidized Bed Gasifier*. PhD thesis, Chalmers University of Technology, Gothenburg, Sweden, 2014.

[28] Roberto Solimene, Antonio Marzocchella, and Piero Salatino. Hydrodynamic interaction between a coarse gas-emitting particle and a gas fluidized bed of finer solids. *Powder Technology*, 133(1-3):79–90, jul 2003.

[29] A Gómez-Barea and B Leckner. Modeling of biomass gasification in fluidized bed, 2010.

[30] I Nyoman Suprapta Winaya, Tadaaki Shimizu, and Daisuke Yamada. A new method to evaluate horizontal solid dispersion in a bubbling fluidized bed. *Powder Technology*, 178(3):173–178, 2007.

[31] Lothar Reh. Development potentials and research needs in circulating fluidized bed combustion. *China Particuology*, 1(5):185–200, 2003.

[32] Teresa Berdugo Vilches. *Operational strategies to control the gas composition in dual fluidized bed biomass gasifiers*. PhD thesis, Chalmers University of Technology, Gothenburg, Sweden, 2018.

[33] Erik Sette, David Pallarès, and Filip Johnsson. Influence of bulk solids cross-flow on lateral mixing of fuel in dual fluidized beds. *Fuel Processing Technology*, 140:245–251, 2015.

[34] Johanna Olsson, David Pallarès, and F Johnsson. Lateral fuel dispersion in a large-scale bubbling fluidized bed. *Chemical Engineering Science*, 74(0):148–159, 2012.

[35] Daoyin Liu and Xiaoping Chen. Lateral solids dispersion coefficient in large-scale fluidized beds. *Combustion and Flame*, 157(11):2116–2124, 2010.

[36] L M Garcia-Gutierrez, A Soria-Verdugo, and U Ruiz-Rivas. Optimization of the feeding ports location in a fluidized bed combustor based on Monte Carlo simulations of fuel particles motion. *Fuel*, 141:82–92, 2015.

[37] Ke Qin, Henrik Thunman, and Bo Leckner. Mass transfer under segregation conditions in fluidized beds. *Fuel*, 195:105–112, 2017.

[38] Louise Lundberg, Placid A Tchoffor, David Pallarès, Robert Johansson, Henrik Thunman, and Kent Davidsson. Influence of surrounding conditions and fuel size on the gasification rate of biomass char in a fluidized bed. *Fuel Processing Technology*, 144:323–333, 2016.

[39] P.N. Rowe, B A Partridge, A G Cheney, G A Henwood, and E Lyall. The mechanisms of solids mixing in fluidised beds. *Chemical Engineering Research and Design*, 43a:271–286, 1965.

[40] I N M Woollard and O E Potter. Solids mixing in fluidized beds. *AIChE Journal*, 14(3):388–391, may 1968.

[41] P.N. Rowe and B A Partridge. An x-ray study of bubbles in fluidised beds. *Chemical Engineering Research and Design*, 75, Supple(0):S116–S134, 1997.

[42] I Eames and M A Gilbertson. Mixing and drift in gas-fluidised beds. *Powder Technology*, 154(2–3):185–193, 2005.

[43] Yan-fu Shi and L T Fan. Lateral mixing of solids in batch gas-solids fluidized beds. *Industrial & Engineering Chemistry, Process Design and Development*, 23(2):337–341, 1984.

[44] J Werther. Bubble chains in large diameter gas fluidized beds. *International Journal of Multiphase Flow*, 3(4):367–381, 1977.

[45] David Pallarès and Filip Johnsson. A novel technique for particle tracking in cold 2-dimensional fluidized beds—simulating fuel dispersion. *Chemical Engineering Science*, 61(8):2710–2720, apr 2006.

[46] D Kunii and O Levenspiel. *Fluidization Engineering*. Butterworth-Heinemann, 1991.

[47] P.N. Rowe and A.W. Nienow. Particle mixing and segregation in gas fluidised beds. A review. *Powder Technology*, 15(2):141–147, nov 1976.

[48] A.W. Nienow, P.N. Rowe, and Tadatoshi Chiwa. Mixing and segregation of a small proportion of large particles in gas fluidized beds of considerably. *AIChE Symposium Series*, 74:45–53, 1978.

[49] Zhihao Yang, Lunbo Duan, Lin Li, Daoyin Liu, and Changsui Zhao. Movement and mixing behavior of a single biomass particle during combustion in a hot fluidized bed combustor. *Powder Technology*, 370:88–95, 2020.

[50] Zhihao Yang, Lunbo Duan, Lin Li, and Edward John Anthony. Movement and combustion characteristics of densified rice hull pellets in a fluidized bed combustor at elevated pressures. *Fuel*, 294:120421, 2021.

[51] Markku Nikku, Kari Myöhänen, Jouni Ritvanen, Timo Hyppänen, and Marko Lyytikäinen. Three-dimensional modeling of biomass fuel flow in a circulating fluidized bed furnace with an experimentally derived momentum exchange model. *Chemical Engineering Research and Design*, 115:77–90, 2016.

[52] Clayton T Crowe, John D Schwarzkopf, Martin Sommerfeld, and Yutaka Tsuji. *Multiphase Flows with Droplets and Particles*. Second edi edition, 2011.

[53] E.-U. Hartge, K Luecke, and J Werther. The role of mixing in the performance of CFB reactors. *Chemical Engineering Science*, 54(22):5393–5407, 1999.

[54] Kari Myöhänen and Timo Hyppänen. A Three-Dimensional Model Frame for Modelling Combustion and Gasification in Circulating Fluidized Bed Furnaces, 2011.

[55] D Pallarès and F Johnsson. 11 - Modeling of fluidized bed combustion processes. In Fabrizio B T Fluidized Bed Technologies for Near-Zero Emission Combustion Scala and Gasification, editors, *Woodhead Publishing Series in Energy*, pages 524–578. Woodhead Publishing, 2013.

[56] Tingwen Li and Yupeng Xu. Computational Fluid Dynamics and Its Application to Fluidization, apr 2020.

[57] Meisam Farzaneh, Srdjan Sasic, Alf Erik Almstedt, Filip Johnsson, and David Pallarès. A study of fuel particle movement in fluidized beds. *Industrial and Engineering Chemistry Research*, 52(16):5791–5805, 2013.

[58] Tingwen Li, Sreekanth Pannala, and Mehrdad Shahnam. CFD simulations of circulating fluidized bed risers, part II, evaluation of differences between 2D and 3D simulations. *Powder Technology*, 254:115–124, 2014.

[59] F Hernández-Jiménez, L M Garcia-Gutierrez, A Soria-Verdugo, and A Acosta-Iborra. Fully coupled TFM-DEM simulations to study the motion of fuel particles in a fluidized bed. *Chemical Engineering Science*, 134:57–66, 2015.

[60] Kaiqiao Wu, Victor Francia, and Marc-Olivier Coppens. Dynamic viscoplastic granular flows: A persistent challenge in gas-solid fluidization. *Powder Technology*, 365:172–185, 2020.

[61] David Pallarès and Filip Johnsson. Modeling of fuel mixing in fluidized bed combustors. *Chemical Engineering Science*, 63(23):5663–5671, 2008.

[62] L Ratschow, R Wischnewski, E.-U. Hartge, and J. Werther. Three-Dimensional Simulation of Temperature Distributions in Large-Scale Circulating Fluidized Bed Combustors. In Guangxi Yue, Hai Zhang, Changsui Zhao, and Zhongyang Luo, editors, *Proceedings of the 20th International Conference on Fluidized Bed Combustion*, pages 780–785, Berlin, Heidelberg, 2010. Springer Berlin Heidelberg.

[63] J F Davidson and D Harrison. Fluidised particles, 1963.

[64] J R Grace and D Harrison. The behaviour of freely bubbling fluidised beds. *Chemical Engineering Science*, 24(3):497–508, 1969.

[65] J R Grace and R Clift. On the two-phase theory of fluidization. *Chemical Engineering Science*, 29(2):327–334, 1974.

[66] J. Werther. Influence of the bed diameter on the hydrodynamics of gas fluidized beds. In *AIChE symposium series*, volume 70, pages 53–62, 1974.

[67] Filip Johnsson, S. Andersson, and B. Leckner. Expansion of a freely bubbling fluidized bed. *Powder Technology*, 68(2):117–123, 1991.

[68] R M Davies and Geoffrey Taylor. The Mechanics of Large Bubbles Rising through Extended Liquids and through Liquids in Tubes. *Proceedings of the Royal Society of London. Series A. Mathematical and Physical Sciences*, 200(1062):375–390, 1950.

[69] Richard C. Darton, RD La Nauze, J F Davidson, and D Harrison. Bubble Growth Due To Coalescence in Fluidized Beds. *Transactions of the Institution of Chemical Engineers*, 55:274–280, 1977.

[70] J. Baeyens and S.Y. Wu. Bed expansion and the visible bubble flow rate in gas fluidized beds. *Advanced Powder Technology*, 3(3):163–189, 1992.

[71] A Soria-Verdugo, L M Garcia-Gutierrez, S Sanchez-Delgado, and U Ruiz-Rivas. Circulation of an object immersed in a bubbling fluidized bed. *Chemical Engineering Science*, 66(1):78–87, 2011.

[72] L M Garcia-Gutierrez, A. Soria-Verdugo, C. Marugán-Cruz, and U. Ruiz-Rivas. Simulation and experimental study on the motion of non-reacting objects in the freeboard of a fluidized bed. *Powder Technology*, 263:112–120, 2014.

[73] Yupeng Xu, Tingwen Li, Liqiang Lu, Sina Tebianian, Jamal Chaouki, Thomas W Leadbeater, Rouzben Jafari, David J Parker, Jonathan Seville, Naoko Ellis, and John R Grace. Numerical and experimental comparison of tracer particle and averaging techniques for particle velocities in a fluidized bed. *Chemical Engineering Science*, 195:356–366, 2019.

[74] Erik Sette, Teresa Berdugo Vilches, David Pallarès, and Filip Johnsson. Measuring fuel mixing under industrial fluidized-bed conditions – A camera-probe based fuel tracking system. *Applied Energy*, 163:304–312, 2016.

[75] Kok S Lim and Pradeep K Agarwal. Circulatory motion of a large and lighter sphere in a bubbling fluidized bed of smaller and heavier particles. *Chemical Engineering Science*, 49(3):421–424, 1994.

[76] Joshua B Drake and Theodore J Heindel. Comparisons of Annular Hydrodynamic Structures in 3D Fluidized Beds Using X-Ray Computed Tomography Imaging. *Journal of Fluids Engineering*, 134(8), aug 2012.

[77] Sina Tebianian, Naoko Ellis, Paola Lettieri, and John R Grace. X-ray imaging for flow characterization and investigation of invasive probe interference in travelling fluidized bed. *Chemical Engineering Research and Design*, 104:191–202, 2015.

[78] Frank Schillinger, Simon Maurer, Martin Künstle, Tilman J Schildhauer, and Alexander Wokaun. Hydrodynamic investigations by a local optical measurement technique designed for high-temperature applications – first measurements at a fluidized bed immersed by vertical internals at cold conditions. *Powder Technology*, 344:849–863, 2019.

[79] Alexander Penn, Christopher M. Boyce, Nicholas Conzelmann, Gaëtan Bezinge, Klaas P. Pruessmann, and Christoph R. Müller. Real-time magnetic resonance imaging of fluidized beds with internals. *Chemical Engineering Science*, 198:117–123, apr 2019.

[80] G M Rios, K Dang Tran, and H Masson. FREE OBJECT MOTION IN A GAS FLUIDIZED BED. *Chemical Engineering Communications*, 47(4-6):247–272, 1986.

[81] M Stein, Y L Ding, J P K Seville, and D J Parker. Solids motion in bubbling gas fluidised beds. *Chemical Engineering Science*, 55(22):5291–5300, 2000.

[82] Farzam Fotovat, Renaud Ansart, Mehrdji Hemati, Olivier Simonin, and Jamal Chaouki. Sand-assisted fluidization of large cylindrical and spherical biomass particles: Experiments and simulation. *Chemical Engineering Science*, 126:543–559, 2015.

[83] C. R.K. Windows-Yule, A. Moore, C. Wellard, D. Werner, D. J. Parker, and J. P.K. Seville. Particle distributions in binary gas-fluidised beds: Shape matters – But not much. *Chemical Engineering Science*, 216:115440, apr 2020.

[84] Xiaona Wang, Max Q.-H. Meng, and Chao Hu. A Localization Method Using 3-axis Magnetoresistive Sensors for Tracking of Capsule Endoscope. 1(3):2522–2525, 2006.

[85] Johannes Neuwirth, Sergiy Antonyuk, Stefan Heinrich, and Michael Jacob. CFD–DEM study and direct measurement of the granular flow in a rotor granulator. *Chemical Engineering Science*, 86(0):151–163, 2013.

[86] G Mohs, O Gryczka, S Heinrich, and L Mörl. Magnetic monitoring of a single particle in a prismatic spouted bed. *Chemical Engineering Science*, 64(23):4811–4825, 2009.

[87] V. Idakiev and L. Mörl. How to measure the particle translation and rotation in a spouted and fluidized bed? *Journal of Chemical Technology and Metallurgy*, 48(5):445–450, 2013.

[88] K A Buist, Alex C van der Gaag, Niels G Deen, and J A M Kuipers. Improved magnetic particle tracking technique in dense gas fluidized beds. *AIChE Journal*, 60(9):3133–3142, 2014.

[89] Jack Halow, Kerri Holsopple, Benjamin Crawshaw, Stuart Daw, and Charles Finney. Observed Mixing Behavior of Single Particles in a Bubbling Fluidized Bed of Higher-Density Particles. *Industrial & Engineering Chemistry Research*, 51(44):14566–14576, 2012.

[90] K A Buist, T W van Erdewijk, N G Deen, and J A M Kuipers. Determination and comparison of rotational velocity in a pseudo 2-D fluidized bed using magnetic particle tracking and discrete particle modeling. *AIChE Journal*, 61(10):3198–3207, 2015.

[91] Erik Sette, David Pallarès, Filip Johnsson, Fredrik Ahrentorp, Anders Ericsson, and Christer Johansson. Magnetic tracer-particle tracking in a fluid dynamically down-scaled bubbling fluidized bed. *Fuel Processing Technology*, 138:368–377, 2015.

[92] L. R. Glicksman, M R Hyre, and P A Farrell. Dynamic similarity in fluidization. *International Journal of Multiphase Flow*, 20(SUPPL. 1):331–386, 1994.

[93] Masayuki Horio, Akira Nonaka, Yoshitaka Sawa, and Iwao Muchi. A new similarity rule for fluidized bed scale-up. *AIChE Journal*, 32(9):1466–1482, sep 1986.

[94] M Stein, Y L Ding, and J P K Seville. Experimental verification of the scaling relationships for bubbling gas-fluidised beds using the PEPT technique. *Chemical Engineering Science*, 57(17):3649–3658, sep 2002.

[95] John Sanderson and Martin J Rhodes. Hydrodynamic similarity of solids motion and mixing in bubbling fluidized beds. *AIChE Journal*, 49(9):2317–2327, sep 2003.

[96] Erik Sette, David Pallarès, and Filip Johnsson. Experimental quantification of lateral mixing of fuels in fluid-dynamically down-scaled bubbling fluidized beds. *Applied Energy*, 136(0):671–681, 2014.

[97] L. R. Glicksman. Scaling relationships for fluidized beds. *Chemical Engineering Science*, 39(9):1373–1379, 1984.

[98] A C Rees, J F Davidson, J S Dennis, and A N Hayhurst. The rise of a buoyant sphere in a gas-fluidized bed. *Chemical Engineering Science*, 60(4):1143–1153, 2005.

[99] Fredrik Niklasson, Henrik Thunman, Filip Johnsson, and Bo Leckner. Estimation of Solids Mixing in a Fluidized-Bed Combustor. *Industrial & Engineering Chemistry Research*, 41(18):4663–4673, 2002.

[100] Winslow H Herschel and Ronald Bulkley. Konsistenzmessungen von Gummi-Benzollösungen. *Kolloid-Zeitschrift*, 39(4):291–300, 1926.

[101] T C Daniels. Density separation in gaseous fluidized beds. *Rheology of Disperse Systems*, 5:211–221, 1959.

[102] D F King, F R G Mitchell, and D Harrison. Dense phase viscosities of fluidised beds at elevated pressures. *Powder Technology*, 28(1):55–58, 1981.

[103] Takami Kai, Masahiro Murakami, Ken ichi Yamasaki, and Takeshige Takahashi. Relationship between apparent bed viscosity and fluidization quality in a fluidized bed with fine particles. *JOURNAL OF CHEMICAL ENGINEERING OF JAPAN*, 24(4):494–500, 1991.

[104] A C Rees, J F Davidson, J S Dennis, and A N Hayhurst. The Apparent Viscosity of the Particulate Phase of Bubbling Gas-Fluidized Beds: A Comparison of the Falling or Rising Sphere Technique with Other Methods. *Chemical Engineering Research and Design*, 85(10):1341–1347, 2007.

[105] P Anjaneyulu and D V Khakhar. Rheology of a gas-fluidized bed. *Powder Technology*, 83:29–34, 1995.

[106] K. Schügerl, M. Merz, and F. Fetting. Rheologische eigenschaften von gasdurchströmten fliessbettsystemen. *Chemical Engineering Science*, 15(1-2):1–38, jul 1961.

[107] J R Grace. The viscosity of fluidized beds. *The Canadian Journal of Chemical Engineering*, 48(1):30–33, 1970.

[108] Alessandro Colafigli, Luca Mazzei, Paola Lettieri, and L G Gibilaro. Apparent viscosity measurements in a homogeneous gas-fluidized bed. *Chemical Engineering Science*, 64(1):144–152, 2009.

[109] Bo Lv, Yanhong Fu, Zhenfu Luo, Bo Zhang, Xingzong Qin, and Xiangnan Zhu. Viscosity and separation performance of a gas-solid separation fluidized beds. *Advanced Powder Technology*, 29(12):3375–3384, 2018.

[110] R. P. Chhabra. *Bubbles, Drops, and Particles in Non-Newtonian Fluids*. CRC Press, 2007.

[111] U.T. Andres. Equilibrium and motion of spheres in a viscoplastic liquid. *Sov. Phys. Dokl. (U.S.A.)*, 5:723, 1960.

[112] P H T Uhlherr, T N Le, and C Tiu. Characterisation of inelastic power-law fluids using falling sphere data. *The Canadian Journal of Chemical Engineering*, 54(6):497–502, dec 1976.

[113] Sadao Hirota and Masao Takada. Analysis of Non-Newtonian Flow by Falling-Sphere Method. *Bulletin of the Chemical Society of Japan*, 32(11):1191–1194, nov 1959.

[114] Albert Einstein. *Investigations on the theory of the Brownian movement.* Dover, 1956.

[115] Xiang Qian, Huang Guoquan, Ni Mingjiang, Cen Kefa, and Tao Tao. Lateral Dispersion of Large Coal Particles in an Industrial-Scale Fluidised Bed Combustor. *Journal of Zhejiang University (Engineering Science)*, (6):69–77, 1987.